Design and Analysis of a Novel Wave Energy Converter With a Tension Leg Platform and Oscillating Proof Masses

by

Franklin Zhang

B.S. in Electrical Engineering and Computer Science, Massachusetts Institute of Technology (2020)

Submitted to the Department of Electrical Engineering and Computer Science
in partial fulfillment of the requirements for the degree of

Master of Engineering in Electrical Engineering and Computer Science

at the

MASSACHUSETTS INSTITUTE OF TECHNOLOGY

February 2022

Author .....
Department of Electrical Engineering and Computer Science
January 14, 2022

Certified by .....
Paul Sclavounos
Professor of Mechanical Engineering and Naval Architecture
Thesis Supervisor

Accepted by .....
Katrina LaCurts
Chair, Master of Engineering Thesis Committee

Design and Analysis of a Novel Wave Energy Converter With a Tension Leg Platform and Oscillating Proof Masses

by

Franklin Zhang

Submitted to the Department of Electrical Engineering and Computer Science
on January 14, 2022, in partial fulfillment of the
requirements for the degree of
Master of Engineering in Electrical Engineering and Computer Science

Abstract

A design of novel wave energy converter with an oscillating proof mass and an electromagnetic power takeoff mechanism was considered. The wave energy converter has two parts, a tension leg platform connected by tether lines to the sea floor and inside of it, proof mass oscillators with motions which are coupled to those of the tension leg platform. In order to simplify the analysis, the system was constrained to only oscillate in the direction of surge. Complex hydrodynamic forces caused by ocean waves will excite the system and the surge motion of the proof mass relative to the tension leg platform will generate power via the electromagnetic power takeoff mechanism. First a model of the system with a linear restoring force exerted on the proof mass is analyzed using linear theory. Following the development of the linear theory, a more complex model with a nonlinear restoring force was considered. Using both a frequency-domain approach and a time-domain simulation, the average power of these systems were calculated. To further maximize power, a control circuit and control law are introduced which increase the average power by multiple factors. By introducing nonlinear restoring force and a control law, the performance of the system was shown to be further improved.

Thesis Supervisor: Paul Sclavounos
Title: Professor of Mechanical Engineering and Naval Architecture

Acknowledgments

I want to thank all the members of the Laboratory for Ship Platform Flows for contributing to this thesis and having interesting technical discussions with me. I want to give a special thanks to David Larson for frequently meeting with me to answer many of my questions about hydrodynamics and giving me advice on doing research. I don't think I would have made it this far without his support and guidance.

I would also like to thank my thesis supervisor Professor Paul Sclavounos for providing helpful feedback and guidance in all stages of this work. Additionally I would like to thank my academic advisor Professor Jing Kong for always being so supportive.

I would like to thank my friends and my housemates for making my time at MIT so special. Lastly I would like to thank my family because if it weren't for all their sacrifices and hard work I wouldn't be where I am today.

Contents

List of Figures

List of Tables

Chapter 1

Introduction

1.1 Problem Statement

The world is experiencing a pivot towards sustainable energy, away from fossil fuels. In this transition, energy sources such as solar, wind, geothermal, hydroelectric are all going to play a role in the transition. Wave energy converters (WECs) could provide a source of renewable energy in certain environments where other sources are not as effective. Wave power is currently not widely employed, but the technology is still in its early stages and has room to grow [9].

In this paper we will consider a wave energy converter that has a tension leg platform (TLP) and inside of it, multiple proof mass oscillators. While many types of wave energy converter designs exist, including oscillating water columns (OWC), oscillating body systems, and overtopping converters, of the oscillating body systems there are not many that consider the type of architecture mentioned earlier [1]. The TLP plus proof mass architecture will be explored to investigate its power harvesting capability. The WEC will have an electromagnetic power take-off mechanism. While harvesters with electromagnetic power take-off mechanism are fairly common, the combination with this wave energy architecture makes a novel design worth exploring [7].

1.2 Use Cases

This wave energy converter design has many potential applications. Solar and wind power take up a lot of land that can otherwise be used for other purposes. Wind also causes visual and sound pollution which means that it would be difficult to build near residential areas. Offshore wind turbines would not have these issues when they are located at a distance from the coastlines. This architecture can be built at a large scale in order to be a power harvesting plant to provide electricity to the grid. Alternatively, at a smaller scale it can be used to provide energy to other marine systems. For example, it can be part of an underwater vehicle layout, allowing it to charge the vehicle's batteries without any human intervention or requiring the vehicle to resurface.

Chapter 2

Background

First we will go over some background before talking about the design of the WEC. This background section will cover topics including hydrodynamics, theory on energy harvesting, controls, electromagnetics and useful software. This section will provide the fundamentals for understanding the subsequent sections.

2.1 Hydrodynamic Forces

The dynamics of WECs are rather complicated due to the interaction between the WEC and the waves. We will go over some of the equations and models used to describe WECs as detailed by Falnes [4]. We will consider a more generic point absorber with no proof masses as the WEC. The sections, 2.11, 2.1.2, and 2.1.3 summarize Falnes's explanations.

2.1.1 Radiation Force

Now let's talk about the forces that act on the WEC in the context of wave and WEC interactions, there are two main forces we are considering, the radiation force and the excitation force. The radiation force $F_R(t)$ is caused by the WEC oscillation in the water radiating waves due to its motions. The frequency domain equation of the radiation force is shown in the equation below.

$$F_R(\omega) = -Z_R(\omega)\Xi(\omega)i\omega \tag{2.1}$$

where $F_R(\omega), Z_R(\omega)$, and $\Xi(\omega)$ are the Fourier transform of the radiation force, radiation impedance, and displacement of the WEC respectively. $Z_R(\omega)$ is a causal system, meaning that the input is the cause of the response and that the impulse response of the system is 0 for $t < 0$.

The radiation impedance can be split up into the radiation resistance term $R_R(\omega)$ and a term containing the added mass function $A(\omega)$ as shown below

$$Z_R(\omega) = R_R(\omega) + i\omega A(\omega) \tag{2.2}$$

$$F_R(\omega) = -\left(R_R(\omega) + i\omega A(\omega)\right)\Xi(\omega)i\omega \tag{2.3}$$

We can further simplify the expression by substituting in a expression including a

function $H_R(\omega)$ for $R_R(\omega)$, where $H_R(\omega)$ is defined as:

$$H_R(\omega) = A(\omega) - A(\infty) + \frac{1}{i\omega} R_R(\omega) \tag{2.4}$$

$$F_R(\omega) = (H_R(\omega) - A(\omega))\, i\omega \Xi(\omega) i\omega \tag{2.5}$$

and another substitution $K_R(\omega) = i\omega H_R(\omega)$ to get the time domain expressions shown in equation 2.6 and 2.7 where $*$ denotes convolution. Where $h_R(t)$ and $k_R(t)$ are the causal time domain impulse response functions of $H_R(\omega)$ and $K_R(\omega)$ respectively. $\xi(t)$ is the displacement of the WEC and the time domain expression for $\Xi(\omega)$. From this derivation, we obtain the time domain expression for the radiation force.

$$F_R(t) = h_R(t) * \ddot{\xi}(t) + A(\infty)\ddot{\xi}(t) \tag{2.6}$$

$$F_R(t) = k_R(t) * \dot{\xi}(t) + A(\infty)\ddot{\xi}(t) \tag{2.7}$$

2.1.2 Excitation Force

The other component of the hydrodynamic forces that will act on the WEC due wave interactions is the excitation force $F_E(t)$. While the radiation force is caused by the forces generated due to waves created by an oscillating body, the excitation force is the force caused an incident wave when the body is fixed.

$$F_E(t) = f_E(t) * s(t) \tag{2.8}$$

Equation 2.8 gives the excitation force where $f_E(t)$ is a non-causal kernel and $s(t)$ is the wave amplitude signal.

Unlike the radiation force, the excitation force is non-causal, meaning that the impulse response does not equal zero for $t < 0$. The intuition behind the non-causality is that the linear system with the output as the excitation force has the undisturbed incident wave elevation at the origin of the body as input. However the wave is already interacting with the body before the wave arrives at the origin of the

TLP, thus knowing the excitation force at a given time requires knowing the wave amplitude signal at some future time. The non-causal nature of the wave interactions hint towards the need for an optimal controller that is non-causal which requires forecasting of the wave amplitude signal.

By understanding the these forces we can model the equations of motion for our own WEC.

2.2 Harvesting Energy from Ocean Waves

The radiation force and excitation force are the key hydrodynamic forces that act on the WEC and also transfer energy to the WEC. Understanding these forces is one thing, but does the transfer of energy work and how can we transfer the most energy as possible? To answer this question we need to better understand the process of wave energy conversion. Wave energy conversion can be intuitively understood in terms of wave interference. In order to absorb energy from the incident wave, energy has to be removed from the waves. WECs can oscillate to generate a wave that radiates from the center of the WEC that act to cancel out the incident wave, thus removing energy. In this sense, a good WEC has to be a good wave maker in order to extract energy from the incident wave. The radiating wave must have the correct phase and amplitude in order to perfectly interfere with the incident wave. This justifies the need for an optimal controller that can allow the WEC to effectively absorb energy. Falnes describes a theoretical upper bound to the energy that can be absorbed [4]. But this upper bound is even less if we consider the power loss due to viscous and other losses.

2.2.1 Optimal Control

The optimal condition is defined to be when the following conditions are satisfied [4].
Condition 1

$$F_L(\omega) = -Z_I^*(\omega)\Xi(\omega)i\omega \tag{2.9}$$

where $Z_I(\omega)$ is the intrinsic mechanical impedance and doesn't include the effects of control and power takeoff, but does include radiation impedance. $F_L(\omega)$ is the Fourier Transform of the load force, where the load force is proportional to the velocity of the TLP and is what produces the useful power that can be harvested. The optimal condition can also be written as:
Condition 2

$$iw\Xi(\omega) = \frac{F_E(\omega)}{2R_I(\omega)} \tag{2.10}$$

where $R_I(\omega) = \frac{Z_I(\omega)+Z_I^*(\omega)}{2}$ and is real. Either of these conditions can be satisfied for control to be considered optimal. Because of the impedance matching condition, the load force $F_L(\omega)$ also has to return some of the energy back into the system due to reactance power.

Conjugate Control

Conjugate control strategy tries to satisfy condition 1 for optimal control. For the condition to be satisfied equation 2.11 has to hold, the load impedance $Z_L(\omega)$ has to equal the conjugate of the intrinsic impedance

$$Z_L(\omega) = Z_I^*(\omega) \tag{2.11}$$

While conjugate control theoretically should extract the maximum power, the control law itself is not realizable in the real world. It is because conjugate control requires complete knowledge of the ocean spectrum and wave amplitude signal. We would need to be able to forecast the wave signal correctly at any time into the future, which is a very difficult task to accomplish. The other issue with conjugate control is that it assumes that the system is linear, but many real life systems including ours are more complex. Some systems have nonlinear displacement constraints and nonlinear restoring forces. To overcome this issue, other control laws must be considered.

Resistive Control

A more practical alternative to conjugate control is resistive control. The control force is simply set to be proportional to the velocity of the system. The velocity of the system can be easily measured or computed to determine the control force, or this can also be done using some sort of mechanical damper. The resistive damping coefficient that relates the control force and velocity can be chosen to maximize the output power. Although simple to implement, resistive control is not optimal in regards to power harvesting.

Model Predictive Control

Model predictive control (MPC) was shown to produce twice as much power as traditional causal control methods [13]. MPC incorporates prediction of the future sea wave using deterministic wave signal prediction. Siyuan and Guang lay out the steps for the implementation:

1. Model Setup
2. Define an optimization problem in terms of the Bellman optimality principle
3. Use backward recursion to calculate optimal control action

Using MPC has a lot of advantages, including that it can take into account state constraints unlike conjugate control, it takes advantage of knowledge of the future wave signal and is an optimal control law unlike resistive control. Unlike conjugate control, MPC can be practically implemented. Instead of requiring all future knowledge of the wave amplitude signal, MPC can be modified to only require a finite forecasting time horizon. While the modified control law is not optimal in the sense of equation 2.9 and 2.10, the control law approaches optimality as the time horizon increases.

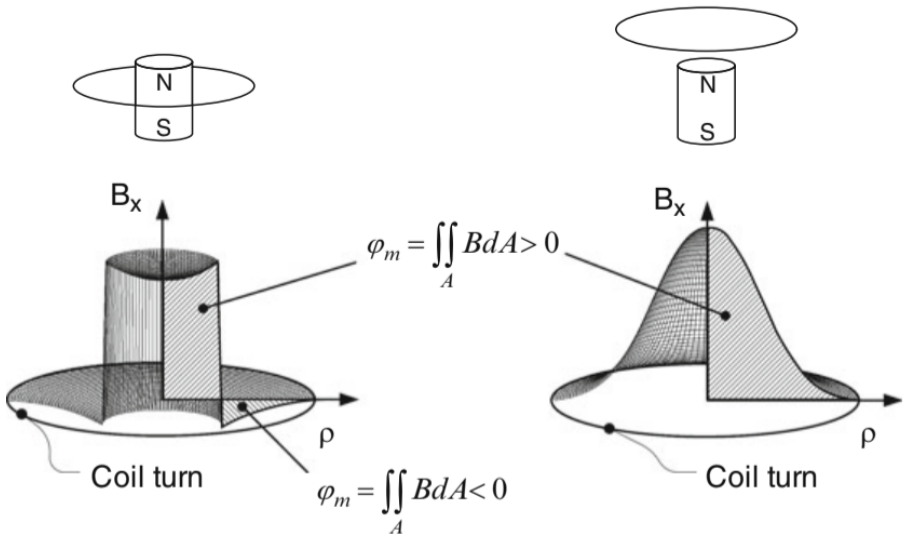

Figure 2-1: The flux through a coil changes with the relative position of the permanent magnet. This image is sourced from [12]

2.3 Electromagnetic Induction

Another important aspect of wave energy conversion that must not be neglected is the power take-off mechanism. We are using an electromagnetic power take-off mechanism. We must understand the theory behind electromagnetic induction because this is what the electromagnetic power take-off mechanism is based upon. In the next few sections we will talk about Faraday's Law of Induction, Lenz's Law, and the magnetic coupling coefficient. While discussing this topic, let us keep in mind that the magnet architecture of interest resembles the one in Figure 2-2.

2.3.1 Faraday's Law of Induction

Faraday's Law of Induction states that the change in magnetic flux through a conductive loop of wire will induce a voltage through that loop [12]. The magnetic flux

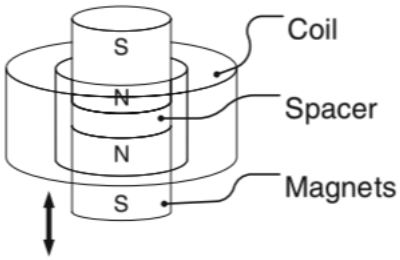

Figure 2-2: This is the architecture for the power take-off mechanism that will be used. A levitating magnet stack with adjacent magnets having opposite polarity and separated by an spacer moves through loops of coil to induce a current. This image is sourced from [12]

is given by equation 2.12

$$\phi_{mag} = \iint_A B_{mag}\, dA$$
$$\text{where } A \text{ is the area enclosed by the wire loop} \tag{2.12}$$
$$\text{and } B_{mag} \text{ is the magnetic flux density}$$

The induced voltage or electromotive force is given by

$$\epsilon_{mag} = -\frac{d}{dt}\phi_{mag} \tag{2.13}$$

2.3.2 Magnetic Coupling

In certain magnet and coil configurations, the magnetic flux changes with respect to some position. Figure 2-1 shows a magnet and coil configuration where the position of the magnet effects the magnetic flux. Magnetic flux is thus a function of the magnet position y. Using the chain rule we can rewrite equation 2.13 to get the equation 2.14

$$\epsilon_m = -\frac{d}{dt}\phi_{mag} = -\frac{d\phi_{mag}}{dy}\frac{dy}{dt} = \gamma_{mag}\dot{y}$$
$$\text{where } \gamma_{mag} \text{ is the magnetic coupling coefficient} \tag{2.14}$$

The magnetic coupling coefficient or also known as the coupling coefficient or transduction factor is key to relating the electromagnetic domain to the mechanical domain. The voltage induced via Faraday's Law will cause a current to flow through the coil. This induced current will produce its own magnetic field which opposes the change in magnetic field via Lenz's law. The magnetic coupling coefficient relates the induced current with the generated force as shown in equation 2.15. Using Ohm's Law, the equation can be rewritten as shown on the right-hand side of equation 2.15, assuming a load resistance in series with the coil. The inductance of the coil loops is often ignored because its contribution is much smaller than that of the resistances and is even smaller at lower frequencies.

$$\begin{gathered} F_i = \gamma_{mag} I_c = \frac{\gamma_{mag}^2}{R_c + R_l}\dot{y} \\ \text{where } F_i \text{ is the induced force} \\ I_c \text{ is the induced coil current} \\ R_c \text{ is the coil resistance} \\ R_l \text{ is the load resistance} \end{gathered} \tag{2.15}$$

2.3.3 Load Power

The power through the load resistance is an important factor to understand. The equation for power is given by equation 2.16

$$P_l = I_l^2 R_l \tag{2.16}$$

To maximize power to the load, impedance matching can be used. The optimal load resistance is given by equation 2.17 [12]. This comes from setting the load resistance equal to the coil resistance and the electrical analog of the viscous mechanical damping term.

$$R_{l,opt} = R_c + \frac{\gamma_{mag}^2}{b_M} \tag{2.17}$$

Experimental analysis has shown that for the architecture in Figure 2-2, the coil

dimensions can be optimized for power [12]. In a study using a two magnet configuration, the power is optimized with a relatively larger magnet radius to coil inner radius and the power is more sensitive to the coil inner radius than to the coil height [12]. This is an important trend to keep in mind while designing the electromagnetic PTO.

2.4 Ocean Spectrum

When harvesting energy from the environment we need to understand and model the environment itself. In this case, we need to understand the ocean spectrum.

$$\begin{gathered} S(\omega) = \frac{5}{16}\frac{\omega_m^2}{\omega^5}H_{1/3}^2 e^{\frac{-5\omega_m^4}{4\omega^4}} \\ \text{where } \omega_m \text{ is the modal frequency} \\ H_{1/3} \text{ is the significant wave height} \end{gathered} \tag{2.18}$$

Equation 2.18 is the Bretschneider Spectrum and is modeled assuming a fully developed sea, meaning that the wind has been blowing over hundreds of miles and for a long time period. The energy of this spectrum is relatively wide-band and has a shallower peak. On the other hand, a JONSWAP Spectrum has a relatively larger peak and more narrow bandwidth. [11]. The model chosen should match that of the spectrum of the ocean at the location where the WEC will be deployed.

The continuous time ocean spectrum from equation 2.18 can be converted into a discrete sum in order to allow the calculation of power to be done computationally. The spectrum within some range ω_{min} to ω_{max} can be approximated as a Riemann sum with K rectangles where the area of the kth rectangle at frequency ω_k is given by the equation 2.19. A wave amplitude signal with this spectrum can be created given K random phase values $\theta_1 \dots \theta_K$ as shown in equation 2.20.

$$\begin{gathered} \Delta S_k = S(\omega_k)\Delta\omega \\ \text{where } \Delta\omega = \frac{\omega_{max} - \omega_{min}}{K} \\ \text{where } \omega_k = \omega_{min} + \Delta\omega\,(k - 1/2) \end{gathered} \tag{2.19}$$

$$\begin{gathered} s(t) = \sum_{k=1}^{K} A_k cos(\omega_k t + \theta_k) \\ A_k = \left[2\Delta\omega S(\omega_k)\right]^{1/2} \end{gathered} \tag{2.20}$$

2.5 Software

Modeling and simulation of certain physical phenomena can be aided with computational tools.

2.5.1 WAMIT

The complex wave-body interactions can be analyzed using a software called WAMIT. WAMIT uses a boundary integral equation method to generate the added-mass and damping coefficients, exciting forces, response-amplitude operators (RAO's), the pressure and fluid velocity, and the mean drift forces and moments for a submerged structure with a given geometry.

2.5.2 FEMM

Modeling of the electromagnetics can be done using finite element methods. FEMM is a free application which solves for the important magnetic parameters such as flux linkage, magnetic flux density and magnetic forces.

Chapter 3

System Overview

The WEC being considered is a tension leg platform TLP, where its inside holds containers with oscillating proof masses. The WEC is categorized as an oscillating point absorber, which means that its dimension is much smaller than the wavelength of the ocean waves and it absorbs energy through its movements near the water surface. The forces of the waves will cause the proof masses to oscillate relative to the TLP. The relative motion of the proof masses will be harvested as energy. The proof mass container is shown in Figure 3-1. In the rest of this paper, WEC will refer to the entire oscillating system including both the TLP and the oscillating proof masses inside it. The TLP will refer to the WEC minus the proof masses. The diagram of the entire WEC is shown in figure 3-2. The WEC can contain multiple proof masses, where M is the number of proof masses. Each proof mass will contain an electromagnetic power take-off mechanism which will convert the mechanical energy of the motion of the proof mass into electricity.

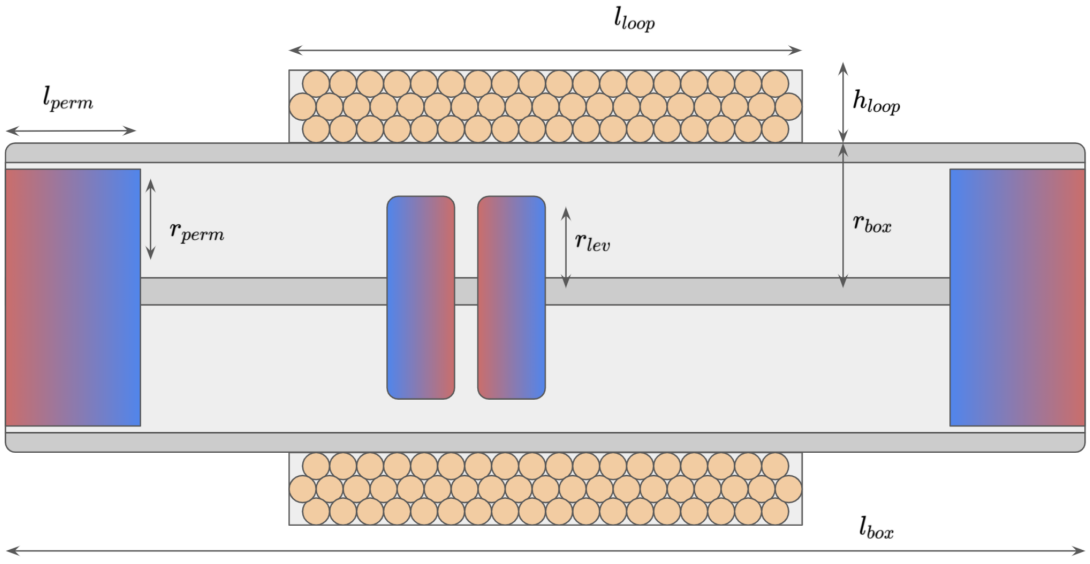

Figure 3-1: Diagram of the oscillating proof mass, including the electromagnetic power take-off mechanism, permanent magnet configuration, and levitating magnet stack. The levitating magnet stack may contain a different number of magnets, but here two are shown. The levitating stack can be connected to a ball bearing mechanism which allows it to slide freely around the container. The magnets in the levitating stack are separated by some distance and that space can contain different ferromagnetic materials such as iron. In the diagram no material is shown. The blue and red colors gradients of the magnets show that adjacent magnets have opposite polarity represented by the change in gradient directions between magnets.

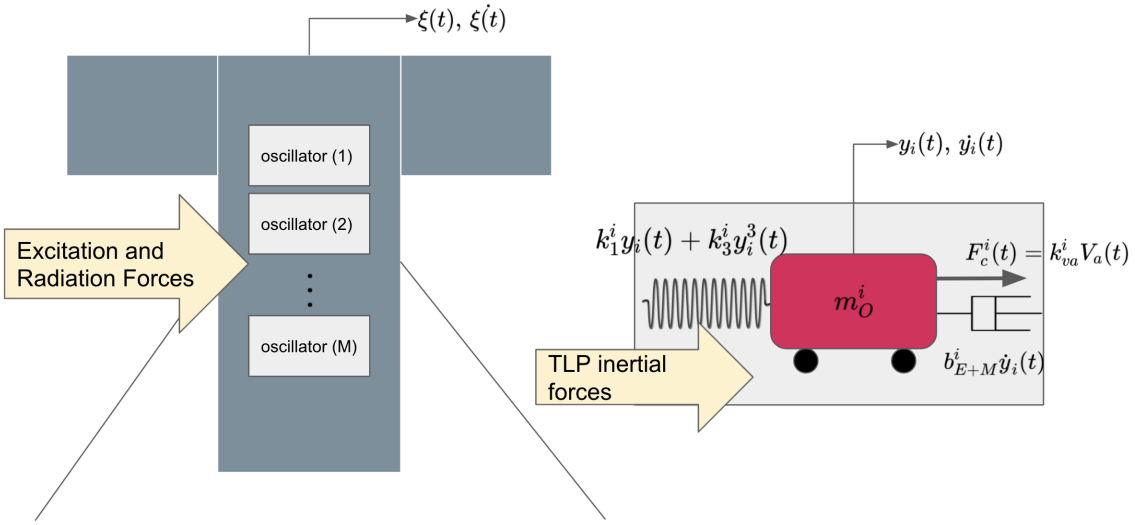

Figure 3-2: Diagram of the WEC, including the TLP and proof mass oscillators. The TLP (shown on the left) is connected to the ocean floor by tethers. These tethers have springs that can be adjusted and their inclination can also be adjusted to control the restoring coefficient of the TLP. The TLP contains up to M number of oscillators and also experience radiation and excitation forces through wave body interactions. On the right is a model of the proof mass oscillator. It is coupled to the TLP so it experiences forces due to the inertial forces of the TLP. Other forces that act on it include the restoring force, damping force, and control force.

3.1 Electromagnetic Power Take-Off

3.1.1 Overview

We will first talk about the power take-off mechanism (PTO). An electromagnetic PTO is being considered because of its efficiency compared to other PTO mechanisms. Each proof mass is oscillating inside a container and the proof mass itself is a group of stacked magnets with opposing poles. The levitating stack contains N_{mag} number of magnets that are stacked very closely together with some separation distance d_{sep}. Loops of coils are wrapped around the container such that motions of the levitating stack are perpendicular to the area of the loops. The motion of the levitating stack causes a change in the magnetic field through the loops, which induces a current through the loops via Faraday's Law of Induction. The induced current also damps the system because it causes a force to act upon the levitating stack magnet.

The coils are connected in parallel to a load path and optionally a controls path. This circuit is shown in Figure 3-3. The coil path contains the loops of coils wrapped around the container and is modeled as a current source in series with the coil resistance R_c, the load path contains a rectifier and a load resister R_l which is where the voltage is turned into power. The last path is the control path which contains a controllable voltage source and a resistor R_a that is used when control is added to the system.

$$I_c = I_l - I_a = \frac{\gamma_{mag}\dot{y}}{R_c} - \frac{R_l}{R_c}\left(\frac{V_a R_c + \gamma_{mag}\dot{y}R_a}{R_c R_a + R_a R_l + R_l R_c}\right) \tag{3.1}$$

The current through the coils is given by equation 3.1. Using the current through the coils, we can calculate the force caused by the induced current as shown in equation 3.2 [12]. The force can then be separated into two terms, one damping term and one control term.

$$\begin{gathered} F_{coils} = \gamma_{mag} I_c = b_E \dot{y} + k_{va} V_a \\ \text{where } b_E = \gamma_{mag}^2 \left[\frac{R_a + R_l}{R_c\left(R_c R_a + R_a R_l + R_l R_c\right)}\right] \\ \text{where } k_{va} = \frac{-\gamma_{mag} R_l}{R_c R_a + R_a R_l + R_l R_c} \end{gathered} \tag{3.2}$$

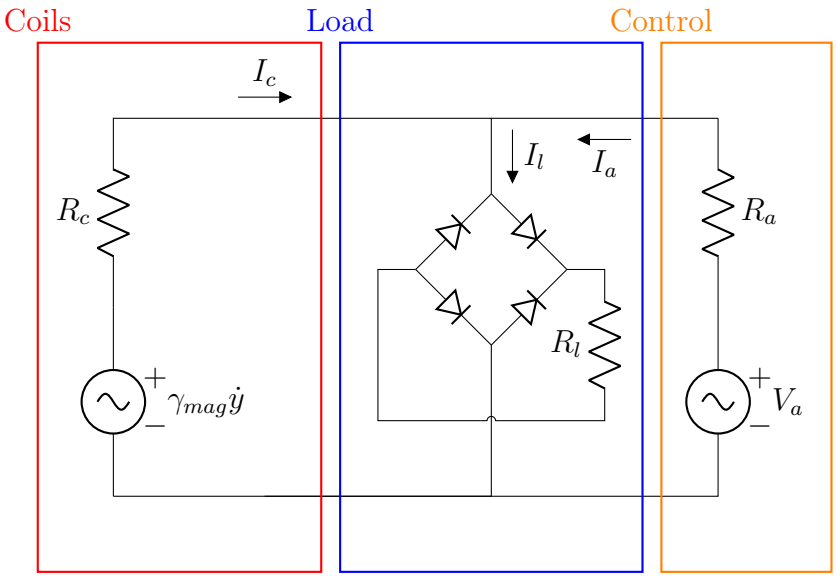

Figure 3-3: Circuit diagram of the power take-off mechanism. Three branches are connected in parallel. The coils branch is in red, load branch in blue and control branch in orange. The coil branch models the loops of coil wrapped around the magnet stack as a voltage source and a resister in series. The load branch contains a load resister and rectifier to extract power. The control branch contains a controllable voltage source and a resister. The control branch can be removed/ignored if using a passive WEC (no control input).

If we don't include a control circuit (that is the same as setting $R_a = \infty$) equation 3.2 simplifies to equation 3.3. Equation 3.1 can be expressed in terms of γ_{mag} and k_{va} as shown in equation 3.4

$$\begin{gathered} F_{coils} = \gamma_{mag} I_c = b_E \dot{y} \\ \text{where } b_E = \frac{\gamma_{mag}^2}{R_c + R_l} \\ \text{where } k_{va} = 0 \\ I_l = \frac{\gamma_{mag} \dot{y}}{R_c + R_l} \end{gathered} \tag{3.3}$$

$$I_c(t) = \frac{1}{\gamma_{mag}} \left(b_E \dot{y}(t) + k_{va} V_a(t) \right) \tag{3.4}$$

3.1.2 Resistances

It is important to calculate and choose the resistances of the PTO circuit. First we can determine the coil resistance R_c. Coil is wrapped around the container holding the proof mass oscillator. There are many different ways to wrap the coils that each have its own advantages [2]. For simplicity, the coil loops will wrap around a certain length of the container centered in the middle and also have multiple layers. Equations 3.5 3.10 describe the calculations for number of loops, current density, total wire length, and total wire resistance given the number of rows and columns of wires.

1. Number of loops:

$$N_{loop} = R_{loop} C_{loop} \tag{3.5}$$

2. Loop length:

$$l_{loop} \tag{3.6}$$

3. Loop height:

$$h_{loop} = r_{wire} \left(2 + \sqrt{3} \left(R_{loop} - 1 \right) \right) \tag{3.7}$$

4. Current Density:

$$J(t) = \frac{N_{loop} I_c(t)}{h_{loop} l_{loop}} \leq J_{max} \tag{3.8}$$

5. Total wire length:

$$l_{wire} = \sum_{i=0}^{R-1} C_{loop} 2\pi (r_{box} + r_{wire}(1 + i\sqrt{3}) = \\ N_{loop} 2\pi (r_{box} + r_{wire}) + 2\pi\sqrt{3} r_{wire} N_{loop}(R_{loop} - 1)/2 \tag{3.9}$$

6. Total resistance of coil loop:

$$R_c = l_{wire}\Omega_{wire} \\ \text{where } \Omega_{wire} \text{ is the resistance per unit length of the wire} \\ \text{with units Ohms per meter.} \tag{3.10}$$

As shown in equation 2.17, the optimal load resistance can be set using impedance matching if we know the coil resistance. If the control branch is included in the circuit, that must also be factored in when implementing the impedance matching for R_l.

3.1.3 Computing the Coupling Coefficient

The coupling coefficient is a key parameter that must be calculated. This can be done with the help of the FEMM software. The FEMM software can calculate the flux linkage through the coils for different configurations. The flux linkage is calculated for different positions of the levitating magnet stack and then the derivative of the flux linkage is found. Figure 3-4 and Figure 3-5 show the input to the FEMM software and the results of having FEMM analyze the input to compute the flux density.

3.1.4 Power Harvested

The instantaneous power through the load resister is given by equation 3.11

$$P_l = I_l^2 R_l = \left(\frac{I_c + V_a/R_a}{1 + R_l/R_a} \right)^2 R_l \tag{3.11}$$

For a system without control ($V_a(t) = 0, R_a = \infty$), the expected energy harvested is given by equation 3.12

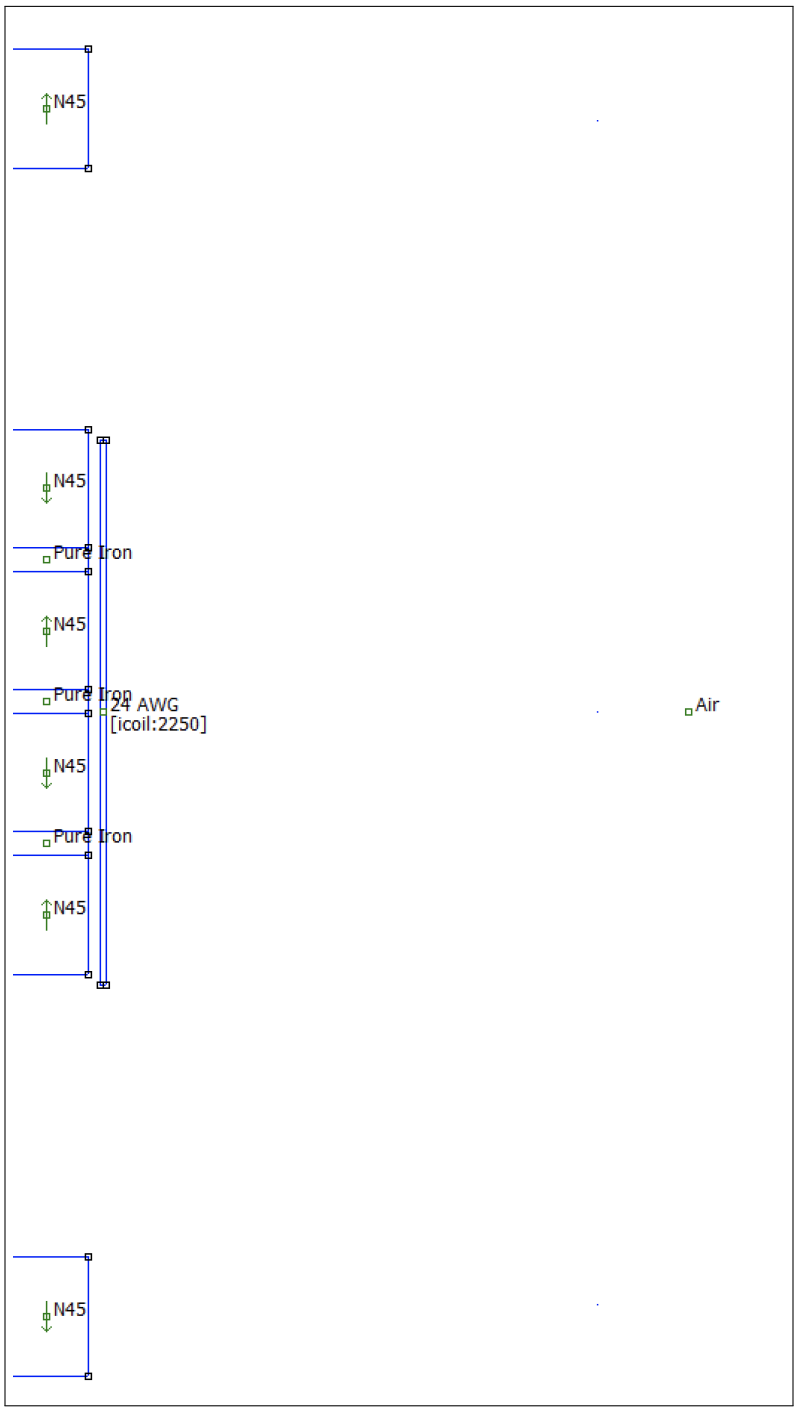

Figure 3-4: The design of the magnetic system to be analyzed using FEMM. This is an example of what the input the to FEMM software could look like. The levitating stack contains 4 magents and pure iron spacers. Permanent side magnets are placed on the ends. The coils are also included as input into FEMM.

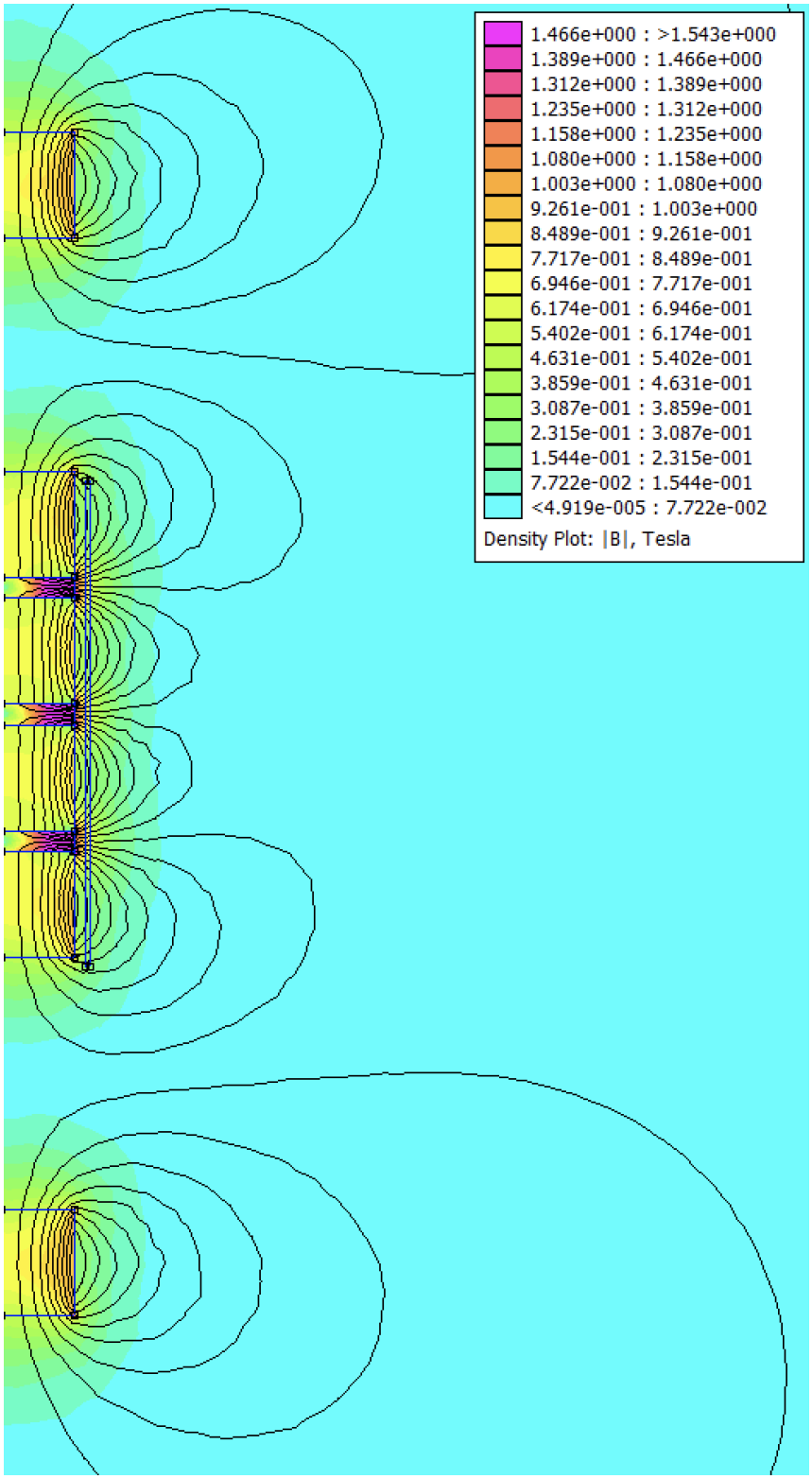

Figure 3-5: Plot of the magnitude of the magnetic flux density using FEMM. This is the result of analyzing the input given in figure 3-4

$$P_{avg} = \left(\frac{\gamma_{mag}}{R_c + R_l}\right)^2 R_l \int_0^\infty \omega^2 S(\omega) \|Y(\omega)\|^2 d\omega \tag{3.12}$$

To get the optimal power P^*_{avg}, we can search over the parameter b_E, the electrical damping coefficient and choose the one that maximizes the power. b^*_E is the optimal electrical damping term. Note that $Y(\omega)$ is now written as a function of b_E as well because the oscillator transfer function is a function of the electrical damping.

$$b_E = \frac{\gamma^2_{mag}}{R_c + R_l} \tag{3.13}$$

$$P^*_{avg} = b^*_E \left(\frac{R_l}{R_l + R_c}\right) \int_0^\infty \omega^2 S(\omega) \|Y(\omega, b^*_E)\|^2 d\omega \tag{3.14}$$

3.2 Tension Leg Platform

Generally the TLP has 6 degrees of freedom, but for simplicity we assume only movement in surge, denoted by the variable $\xi(t)$. The TLP has a variety of forces acting upon it. First is the radiation force which consists of the convolution term and the infinite added mass term A_∞ times the acceleration. The excitation force $F_E(t)$ caused by the waves also affects the TLP. The TLP is attached to the ocean floor with tethers and feels a restoring force $-C_{11}\xi$. Lastly the oscillators inside the TLP exert a force onto the TLP, given by $F_O(t)$

3.2.1 TLP Restoring Force and Tethers

The TLP is attached to the ocean floor by tethers which introduce a linear restoring force equal to $-C_{11}\xi$. The tethers are attached diagonally such that the angle between the tether line and the ocean floor is given by θ_{tether}. If the tether has a spring constant k_{tether}, the restoring coefficient acting on the TLP will be given by equation 3.15

$$C_{11} = 2k_{tether}\cos^2(\theta_{tether}) \tag{3.15}$$

3.2.2 Equation of Motion

Putting all these forces together, we get that the equation that governs the motion of the TLP given by equation 3.16

$$\begin{gathered}(M + A_\infty)\ddot{\xi}(t) + \int_{-\infty}^{t} \dot{\xi}(\tau)k_R(t-\tau)d\tau + C_{11}\xi(t) = F_E(t) + F_O(t) \\ \text{where the force of the oscillators is} \\ F_O(t) = \sum_{i=1}^{M} k_1^i y_i + k_3^i y_i^3 + b_{EM}^i \dot{y}_i + k_{va}^i V_a^i(t)\end{gathered} \tag{3.16}$$

where b_{EM}^i is the combined mechanical and electromagnetic damping

3.3 Linear Oscillator

3.3.1 Equations of Motion

The equation of motion of one of the M proof mass oscillators is given by equation 3.17. The forces acting on the proof mass include the electrical and mechanical damping, the 3rd order nonlinear restoring force, the force introduced by the controls, and the inertial force of the TLP. However, for a linear oscillator with no control, some of the terms are set to zero and we get equation 3.18

$$m\ddot{y} + (b_E + b_M)\dot{y} + k_1 y + k_3 y^3 + k_{va} V_a(t) = -m\ddot{\xi}(t) \tag{3.17}$$

$$m\ddot{y} + (b_E + b_M)\dot{y} + k_1 y = -m\ddot{\xi}(t) \tag{3.18}$$

3.3.2 Frequency Domain Equations of Motion

The frequency domain equation of motion of the proof mass oscillator is given by equation 3.19.

$$Y(\omega) = \frac{m\omega^2 \Xi(\omega)}{-m\omega^2 + b_{EM} i\omega + k_1} \tag{3.19}$$

the frequency domain equation of motion of the TLP given a linear oscillator is given by equation 3.20.

$$\begin{aligned} \Xi(\omega)\Big[-(M + A_\infty)\omega^2 + i\omega B(\omega) + C_{11}\Big] = \\ F_E(\omega) + \sum_{i=1}^{M} Y_i(\omega)[k_1^i + i\omega b_{EM}^i] \end{aligned} \tag{3.20}$$

Equations 3.19 and 3.20 can be combined to obtain equation 3.21, the combined oscillator and TLP equation of motion.

$$\begin{aligned} \Xi(\omega)\Bigg[-(M + A_\infty)\omega^2 + i\omega B(\omega) + C_{11} - \sum_{i=1}^{N} m_i\omega^2 \frac{k_1^i + i\omega b_{EM}^i}{-m_i\omega^2 + b_{EM}^i i\omega + k_1^i}\Bigg] \\ = F_E(\omega) \end{aligned} \tag{3.21}$$

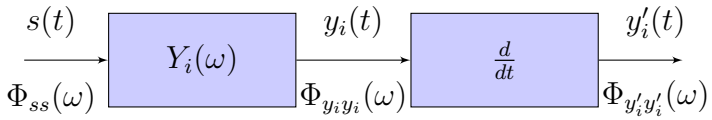

Figure 3-6: Diagram relating the wave amplitude signal $s(t)$ to the relative velocity of the proof mass oscillator.

3.3.3 Statistics

We can next use statistics to model the behaviour of the linear system in a stochastic seastate environment.

Power Spectral Density

The power spectral density (PSD) is useful for calculating variance and mean values for power. It can be derived from the known PSD function of the input seastate and from analyzing the Linear Time Invariant (LTI) system from $s(t)$ to $y_i'(t)$, where $s(t)$ is the input wave signal, $y_i(t)$ is the displacement of the i-th proof mass is response to $s(t)$, and $y_i'(t)$ is the velocity of the i-th proof mass in response to $s(t)$. The variables $\Phi_{ss}(\omega)$, $\Phi_{y_i y_i}(\omega)$, $\Phi_{y_i' y_i'}(\omega)$ are the PSD of $s(t)$, $y_i(t)$, and $y_i'(t)$ respectively. This relationship is shown in figure 3-6 [10]. Equations 3.22 and 3.23 show the relationship between the power spectral densities of motions of the proof mass and the wave amplitude signal. The PSD of the wave amplitude signal can be related back to the spectrum with equation 3.24.

$$\Phi_{y_i y_i}(\omega) = \|Y_i(\omega)\|^2 \Phi_{ss}(\omega) \tag{3.22}$$

$$\Phi_{y_i' y_i'}(\omega) = \omega^2 \|Y_i(\omega)\|^2 \Phi_{ss}(\omega) \tag{3.23}$$

Wave spectrum and wave PSD relationship

$$S(\omega) = \begin{cases} \frac{1}{\pi}\Phi_{ss}(\omega) & \text{if } \omega \geq 0 \\ 0 & \text{if } \omega < 0 \end{cases} \tag{3.24}$$

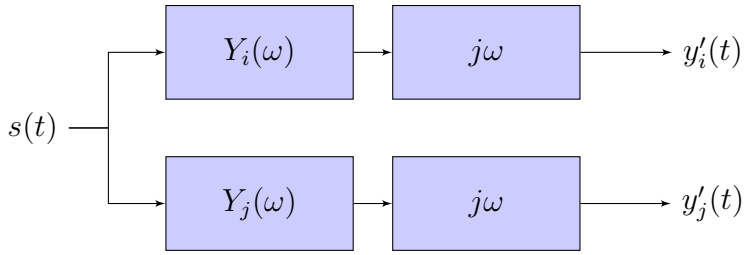

Figure 3-7: System diagram of the LTI systems relating $s(t)$, $y_i'(t)$, and $y_j'(t)$

Cross Power Spectral Density

The complex cross power spectral density (CPSD) is useful for finding the covariance. The CPSD can derived given the transfer function $H_{ij}(\omega)$, relating $y_i'(t)$ to $y_j'(t)$ and the PSD of $y_i'(t)$ [10]. The system block diagram is shown in diagram 3.3.3. We can derive the complex cross spectral density between variables $y_i'(t)$ and $y_j'(t)$ as the expression shown in equation 3.25, where $*$ denotes complex conjugation.

$$\begin{aligned} \Phi_{y_j' y_i'}(\omega) &= \left[\frac{Y_i(\omega)}{Y_j(\omega)}\right]^* \Phi_{y_j' y_j'(\omega)} \\ \Phi_{y_i' y_j'}(\omega) &= \left[\frac{Y_i(\omega)}{Y_j(\omega)}\right] \Phi_{y_j' y_j'(\omega)} \end{aligned} \tag{3.25}$$

we can rewrite the CPSD in terms of the PSD of the wave spectrum

$$\Phi_{y_i' y_j'}(\omega) = \left[\frac{Y_i(\omega)}{Y_j(\omega)}\right] \omega^2 Y_j(\omega) Y_j^*(\omega) \Phi_{ss}(\omega) = \omega^2 Y_i(\omega) Y_j^*(\omega) \Phi_{ss}(\omega) \tag{3.26}$$

Statistics of Displacement

The mean displacement and velocity of the proof mass is zero because the wave amplitude signal $s(t)$ is a zero-mean Gaussian random process. With the mean known, the variances need to be calculated. Taking the integral of the PSD and CPSD allows us to calculate variances and covariances of the displacement and velocity of the proof mass as shown in equations 3.27 to 3.30.

1. Variance of displacement of a proof mass

$$\mathrm{Var}\big(y\big) = \frac{1}{\pi}\int_{-\infty}^{\infty} \Phi_{ss}(\omega)\|Y(\omega)\|^2 d\omega = \int_{0}^{\infty} S(\omega)\|Y(\omega)\|^2 d\omega \tag{3.27}$$

2. Variance of velocity of displacement of a proof mass

$$\mathrm{Var}\big(y_i'\big) = \frac{1}{\pi}\int_{-\infty}^{\infty} \omega^2\|Y_i(\omega)\|^2 \Phi_{ss}(\omega) d\omega = \int_{0}^{\infty} \omega^2 S(\omega)\|Y_i\omega\|^2 d\omega \tag{3.28}$$

3. Covariance of zero-mean, relative velocity of displacements $y_i'(t)$ and $y_j'(t)$. Where $\Re$ denotes the real part.

$$\mathrm{Cov}(y_i', y_j') = E\big[y_i' y_j'\big] = \Re\left(\frac{1}{2\pi}\int_{-\infty}^{\infty} \Phi_{y_i' y_j'}(\omega) d\omega\right)$$
$$= \Re\left(\frac{1}{2\pi}\int_{-\infty}^{\infty} \omega^2 Y_i(\omega) Y_j^*(\omega)\Phi_{ss}(\omega) d\omega\right) = \Re\left(\int_{0}^{\infty} \omega^2 Y_i(\omega) Y_j^*(\omega) S(\omega) d\omega\right) \tag{3.29}$$

We can calculate the complex covariance using a discrete sum, which is given by

$$\mathrm{Cov}(y_i', y_j') = \Re\left(\frac{1}{2}\sum_{k=1}^{K} \omega_k^2 Y_i(\omega) Y_j^*(\omega) A_k^2\right) \tag{3.30}$$

Power Harvested for a Single Proof Mass

The average of power for a WEC with a single proof mass with no control ($R_a = \infty, V_a = 0$) can be calculated. This expression can then be generalized for multiple proof masses.

1. Instantaneous power harvested by a single proof mass is given by equation 3.31.

This is also the power through the load resister.

$$
\begin{gathered}
P_l(t) = I_l^2 R_l = \left(\frac{\gamma_{mag}\dot{y}}{R_c + R_l}\right)^2 R_l = \\
\left(\frac{R_l}{R_c + R_l}\right) b_E \dot{y}^2 = b_{PTO}\dot{y}^2 \\
\text{where } b_E = \frac{\gamma_{mag}^2}{R_c + R_l} \\
\text{where } b_{PTO} = \left(\frac{R_l}{R_c + R_l}\right) b_E
\end{gathered}
\tag{3.31}
$$

2. Mean power harvested by a single proof mass in a given spectrum

$$
\begin{gathered}
\mu_P = b_{PTO}\mathrm{Var}\big(y'\big) \\
= \frac{b_{PTO}}{\pi}\int_{-\infty}^{\infty} \omega^2 \|Y(\omega)\|^2 \Phi_{ss}(\omega) d\omega \\
= b_{PTO}\int_{0}^{\infty} \omega^2 S(\omega)\|Y(\omega)\|^2 d\omega \\
\mu_P = \frac{b_{PTO}}{2}\sum_{k=1}^{K} \omega_k^2 A_k^2 \|Y(\omega_k)\|^2
\end{gathered}
\tag{3.32}
$$

3. Variance in power harvested by a single proof mass

$$
\begin{gathered}
\mathrm{Var}(P(t)) = b_{PTO}^2 E\big[y'^4\big] - \mu_P^2 \\
= 3b_{PTO}^2\left[\frac{\mu_P}{b_{PTO}}\right]^2 - \mu_P^2 = 2\mu_P^2
\end{gathered}
\tag{3.33}
$$

where the 4th moment can be written in terms of the 2nd moment

$$
E[(y')^4] = 3\mathrm{Var}(y')^2 = 3\left[\frac{\mu_P}{b_{PTO}}\right]^2 \tag{3.34}
$$

Power Harvested for M Number of Proof Masses

1. Mean power harvested from N harvesters in a given wave spectrum $S(\omega)$

$$E[P_{tot}] = \sum_{i=1}^{M} E[P_i] = \sum_{i=1}^{M} \mu_{P_i}$$

$$= \sum_{i=1}^{M} \frac{b_{PTO,i}}{\pi} \int_{-\infty}^{\infty} \omega^2 \|Y_i(\omega)\|^2 \Phi_{ss}(\omega) d\omega = \sum_{i=1}^{M} b_{PTO,i} \int_{0}^{\infty} \omega^2 S(\omega) \|Y_i(\omega)\|^2 d\omega$$

This integral can be converted into a summation

$$\mu_{P_{tot}} = \sum_{k=1}^{K} \sum_{i=1}^{M} \frac{b_{PTO,i}}{2} \omega_k^2 A_k^2 \|Y_i(\omega_k)\|^2 \tag{3.35}$$

2. Variance in total power harvested by N proof masses

$$\mathrm{Var}\big(P_{tot}(t)\big) = E\big[P_{tot}^2\big] - E\big[P_{tot}\big]^2 = \sum_{i=1}^{M} \sum_{j=1}^{N} \left\{ b_{PTO,i} b_{PTO,j} E\big[\big(y_i' y_j'\big)^2\big] \right\} - \left(\sum_{k=1}^{M} \mu_{P_k} \right)^2$$

$$= \sum_{i=1}^{M} \sum_{j=1}^{M} \left\{ b_{PTO,i} b_{PTO,j} \left[\frac{\mu_{P_i}}{b_{PTO,i}} + \frac{\mu_{P_j}}{b_{PTO,j}} + 2 \left\| \int_0^{\infty} \omega^2 Y_i(\omega) Y_j^*(\omega) S(\omega) d\omega \right\|^2 \right] \right\} - \left(\sum_{k=1}^{M} \mu_{P_k} \right)^2 \tag{3.36}$$

using a discrete sum we get

$$\mathrm{Var}\big(P_{tot}(t)\big) = \sum_{i=1}^{M} \sum_{j=1}^{M} \left\{ b_{PTO,i} b_{PTO,j} \left[\frac{\mu_{P_i}}{b_{PTO,i}} + \frac{\mu_{P_j}}{b_{PTO,j}} + \frac{1}{2} \left\| \sum_{k=1}^{K} \omega_k^2 Y_i(\omega) Y_j^*(\omega) A_k^2 \right\|^2 \right] \right\} - \left(\sum_{m=1}^{M} \mu_{P_m} \right)^2 \tag{3.37}$$

The term, $E\left[\left(y_i'y_j'\right)^2\right]$ was expanded using the Isserlis' theorem for higher order moments.

$$E\left[\left(y_i'y_j'\right)^2\right] = \mathrm{Var}\left(y_i'\right)\mathrm{Var}\left(y_j'\right) + 2\mathrm{Cov}\left(y_i', y_j'\right)^2 \tag{3.38}$$

3.4 Non-Linear Oscillator

While the linear oscillator is easy to analyze with linear theory and frequency domain analysis, in real life the system will not be a simple linear system. There are some benefits of having a nonlinear system so there is reason to introduce these non-linearities. Non-linearities can be introduced to increase the bandwidth of the harvester and increase the harvested power [7]. To introduce these non-linearities, the restoring spring can be replaced with permanent magnets mounted at the inside ends of the container. The force due to the magnets can be modeled using higher order polynomials. By choosing to use a 3rd order approximation of the restoring force, our oscillator is now a Duffing oscillator. The 1st order restoring force is replaced with a restoring force given by equation 3.39. An optional control branch can also be added to the system.

$$F_{restoring} = -k_1 y - k_3 y^3 \tag{3.39}$$

3.4.1 Equations of Motion

The equations of motion for a non-linear WEC with multiple harvesters and controls are given by equation 3.40 and 3.41.

$$\begin{aligned}(M + A_\infty)\ddot{\xi} + \int_{-\infty}^{t} \dot{\xi} K(t-\tau)d\tau + C_{11}\xi \\ = F_e(t) + \sum_{i=1}^{N} k_1^i y_i + k_3^i y^3 + b_{EM}^i \dot{y}_i + k_{va}^i V_a^i(t)\end{aligned} \tag{3.40}$$

$$m\ddot{y} + (b_E + b_M)\dot{y} + k_1 y + k_3 y^3 + k_{va} V_a(t) = -m\ddot{\xi}(t) \tag{3.41}$$

3.4.2 Magnetic Restoring Force

The magnetic restoring force can be modeled using the FEMM software. The software can be used to calculate the force using the change in the coenergy of the magnetic field when the levitating stack magnet is perturbed by a small amount. This can be done at multiple locations of the levitating magnet stack, then a 3rd order polynomial

can be fit to the data using a least squares method. This would give us the k_1 and k_3 values for the restoring force.

3.4.3 Bi-stable Well

The potential $U(y,t)$ of the non-linear oscillator is given by equation 3.42. For a positive value of k_3 and negative value of k_1, the potential has two stable points, and is called the bi-stable potential. A well designed potential well can make the system behave in a desired manner. The choice of k_1 and k_3 can determine the locations of the stable points y_{stable} and the barrier height ΔU. We can decide on a value for $\dot{y}_{barrier}$ which is the velocity associated with the energy required to cross the barrier. These two conditions given by equation 3.43 and 3.44 can then be used to choose our k_1 and k_3 values.

$$\begin{aligned} F_{restoring} = -\frac{dU}{dy}(y,t) = -k_1 y - k_3 y^3 \\ U(y,t) = \frac{1}{2}k_1 y^2 + \frac{1}{4}k_3 y^4 \end{aligned} \tag{3.42}$$

$$\begin{aligned} \frac{dU}{dy} = k_1 y + k_3 y^3 = 0 \\ k_3 = \frac{-k_1}{y_{stable}^2} \end{aligned} \tag{3.43}$$

$$\begin{aligned} \Delta U = U_{barrier} - U_{stable} = \left(\frac{k_1^2}{4k_3}\right) \\ = \Delta K.E. = \frac{1}{2}m\dot{y}_{barrier}^2 \end{aligned} \tag{3.44}$$

Apply stable point location constraint from 3.43 to give us

$$k_1 = \frac{-4\Delta U}{y_{stable}^2}$$

We can use this idea to design a theoretical well with desired characteristics, but in reality we don't have direct control over what the k_1 and k_3 values are. These are determined by the geometries and physics of the permanent and levitating magnets.

3.5 Controls

To further increase power harvested, controls can be implemented to regulate the system to behave in a desired way. The power harvested is further increased when the oscillator moves in a square wave like manner where it stays at the ends of the box and is held there before traveling very fast to the other end [5]. To implement this we need to have a controllable system.

3.5.1 Control Circuit

An additional branch can be added to the circuitry to allow the system to be controlled. This branch which contains a resister R_a and a controllable voltage source V_a, labeled the control branch, is shown in figure 3-3. The voltage introduces a current through the coils, which induces a force on the oscillators, and the voltage is related to the force through the coefficient k_{va}.

3.5.2 Control Law

To make the system behave in the desired square pulse like manner, we need to send the appropriate voltages. Hosseinloo introduces a simple control law that is called the buy-low-sell-high control law that implements this strategy [6]. The strategy is to apply no control force when the inertial force from the TLP on the oscillator is pushing the proof mass further towards the edge of the container. Then wait until the net force changes signs and wants to force the proof mass towards the opposite direction exerting a control force. This control force will lower the barrier height of the bi-stable well to allow the proof mass to easily swing from one end of the container to the other. The control law is detailed below.

1. Force Left: $V_a(t) > 0$ when $\dot{F}(t) = 0$ and $F(t)x(t) < 0$ and $F(t) < 0$
2. Force Right: $V_a(t) < 0$ when $\dot{F}(t) = 0$ and $F(t)x(t) < 0$ and $F(t) > 0$
3. Trap: $V_a(t) = 0$ when $|x(t)| \approx x_{max}$ and $F(t)x(t) > 0$

3.6 State-Space Modeling

To have confidence that our WEC is designed correctly we must simulate the system. The standard way to do this is to cast the system into a state-space form. Working with state-space models is a well researched and explored area and we can leverage the existing tools in order to understand and analyze our system. We can use state-space models to do time domain simulations, test control strategies, do stability analysis, design control laws, and much more. Getting the system into a state-space form requires knowledge of the equations of motion, some which have already been identified. The resulting continuous and discrete time state-space models are given by equation 3.45 and 3.46 respectively.

$$\begin{aligned} \dot{\mathbf{x}}_{\mathbf{sys}}(t) &= \mathbf{A}_{\mathbf{sys}}\mathbf{x}_{\mathbf{sys}}(t) + \mathbf{B}_{\mathbf{sys}}\mathbf{u}_{\mathbf{sys}}(t) \\ \mathbf{y}_{\mathbf{sys}} &= \mathbf{C}_{\mathbf{sys}}\mathbf{x}_{\mathbf{sys}}(t) + \mathbf{D}_{\mathbf{sys}}\mathbf{u}_{\mathbf{sys}}(t) \end{aligned} \tag{3.45}$$

$$\begin{aligned} \dot{\mathbf{x}}_{\mathbf{sys}}[n+1] &= \mathcal{A}_{\mathbf{sys}}\mathbf{x}_{\mathbf{sys}}[n] + \mathcal{B}_{\mathbf{sys}}\mathbf{u}_{\mathbf{sys}}[n] \\ \mathbf{y}_{\mathbf{sys}} &= \mathcal{C}_{\mathbf{sys}}\mathbf{x}_{\mathbf{sys}}[n] + \mathcal{D}_{\mathbf{sys}}\mathbf{u}_{\mathbf{sys}}[n] \end{aligned} \tag{3.46}$$

3.6.1 Radiation Force

The radiation force is given as the convolution of the velocity of the TLP and the causal radiation kernel $k_R(t)$ as shown in equation 3.47. This convolution is difficult to integrate into a state-space model directly because convolution is a nonlinear operation. We can use system identification in order to turn the nonlinear convolution operation into a linear state-space model like shown in equation 3.48.

$$F_R(t) = \int_{-\infty}^{t} k_R(t-\tau)\dot{\xi}(\tau)d\tau \tag{3.47}$$

$$\begin{aligned} \dot{\mathbf{x}}_{\mathbf{R}} &= \mathbf{A}_{\mathbf{R}}\ \mathbf{x}_{\mathbf{R}} + \mathbf{B}_{\mathbf{R}}\ \dot{\xi(t)} \\ F_R(t) &= \mathbf{C}_{\mathbf{R}}\ \mathbf{x}_{\mathbf{R}} \end{aligned} \tag{3.48}$$

$$\frac{F_R(\omega)}{\Xi(\omega)i\omega} = Z_R(\omega) = K_R(\omega) - i\omega[A(\omega) - A(\infty)] \tag{3.49}$$

$$Z_R(\omega) \approx \mathbf{C_R}(s\mathbf{I} - \mathbf{A_R})^{-1}\mathbf{B_R} \tag{3.50}$$

We need to find the $Z_R(\omega)$, the radiation impedance transfer function relating $\dot{\xi}(t)$ to $F_R(t)$. This is shown in equation 3.49. Then convert that transfer function into an approximate state-space form as shown in equation 3.50. There are two approaches to doing this that can be followed. A MATLAB toolbox called Marine Systems Simulator can take as input the output of WAMIT to create a vessel object. With a built in function, the state-space model of the radiation force can then be obtained from the vessel object. The other method is using MATLAB's control systems toolbox and system identification toolbox. Using WAMIT's output, we obtain samples of the transfer function $Z_R(\omega)$. We can use system identification in the frequency domain to compute the transfer function.

The radiation impedance function was found and a plot is shown in figure 3-8. The system identification toolbox in MATLAB was used to find a model to fit the data. Figure 3-9 shows the convergence of the models identified as the system order increases. Figure 3-10 shows the comparison of the identified system and the frequency domain data of $Z_R(\omega)$.

Although the system in the frequency domain matched the data given, the system is unstable and has poles on the right half plane. To correct for this we can flip the poles along the imaginary axis to convert it into a stable system.

3.6.2 Excitation Force

The excitation force can also be cast into a state-space form using system identification. The frequency domain transfer function for the excitation force is given by $Z_E(\omega)$. The inverse Fourier Transform of $Z_E(\omega)$ gives the excitation force kernel $f_E(t)$ as shown in equation 3.51. $f_E(t)$ relates the wave amplitude signal $s(t)$ to the excitation force $F_E(t)$ as shown in equation 3.52.

$$\mathcal{F}\{f_E(t)\} = Z_E(\omega) \tag{3.51}$$

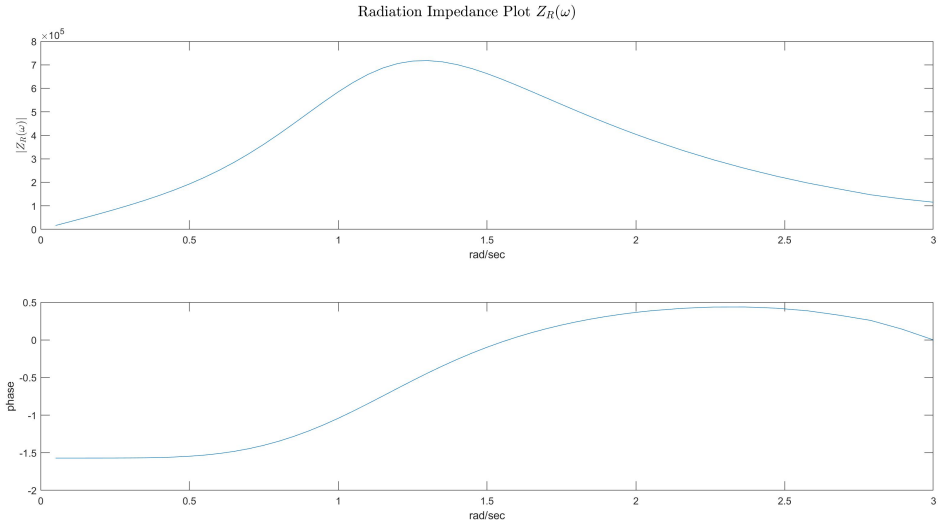

Figure 3-8: Amplitude and phase plot of the radiation impedance function

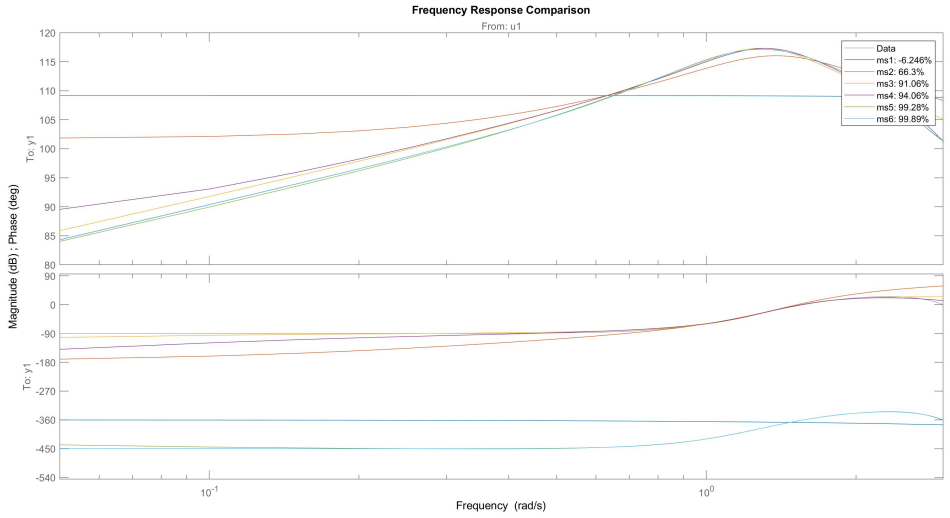

Figure 3-9: Plotting of the frequency domain response of system identification on the radiation impedance function $Z_R(\omega)$ with different system orders. msi represents the identified system with order i. Percentages in the legend show the percent match. For higher orders, the results of the identified system approaches that of the supplied radiation impedance data.

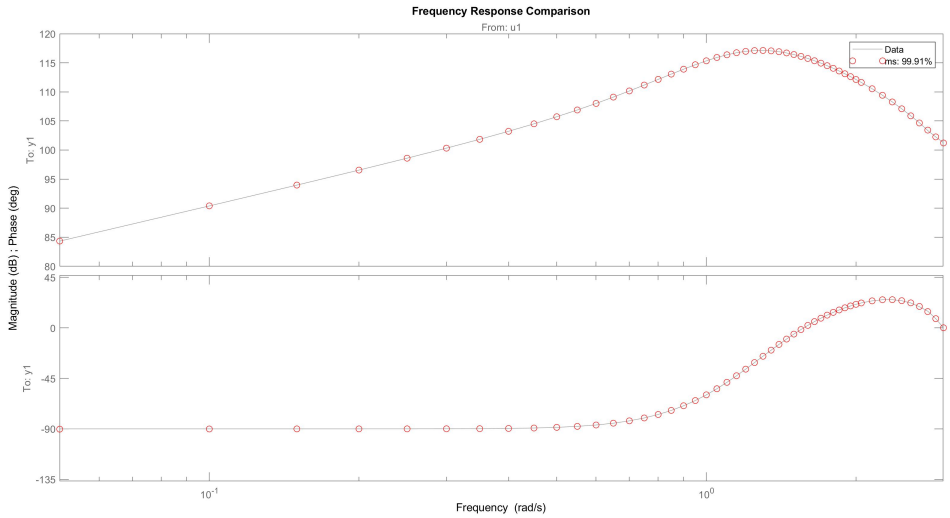

Figure 3-10: Comparison of identified system and the frequency domain data of $Z_R(\omega)$ shows a close match. The red circles show the plot of the identified system while the dark line is the plot of the supplied radiation impedance data.

$$F_E(t) = (f_E * s)(t) \tag{3.52}$$

The excitation force kernel is non-causal, thus making it more difficult to work with[4]. We can take advantage of the fact that for some t_c, $f_E(t) \approx 0$ when $t < -t_c$. This allows us to causalize the kernel by introducing a delay term t_c as shown in equation 3.53. Similarly to what we did for the radiation kernel, we can then use system identification to fit the causalized impulse response function to a state-space model in order to linearize it. The state-space approximation of the excitation force is shown in equation 3.54. This approximation allows us to calculate the excitation force if we know values of the wave amplitude signal up to t_c seconds into the future [3].

$$f_{EC}(t) = f_E(t - t_c) \tag{3.53}$$

$$\begin{aligned} \dot{\mathbf{x}}_{\mathbf{EC}} &= \mathbf{A}_{\mathbf{EC}}\ \mathbf{x}_{\mathbf{EC}} + \mathbf{B}_{\mathbf{EC}}\ s(t + t_c) \\ F_E(t) &= \mathbf{C}_{\mathbf{EC}}\ \mathbf{x}_{\mathbf{EC}} \end{aligned} \tag{3.54}$$

3.6.3 System State-Space Model

For each of the M proof masses and the one TLP, we will have 2 states, the position and velocity for a total of $2M+2$ states. The number of total states in our WEC system is $2M+2+O$ where O is the order of the state-space model for the radiation force. $2M+2+O$ differential equations, one for each state will be combined into a matrix form. The input of the system is given by equation 3.55. The compact equation of the state-space model is shown in equation 3.56 and the expanded form is shown in equation 3.57.

$$\mathbf{u_{sys}}(t) = \begin{bmatrix} F_E(t) \\ V_{a,1}(t) \\ \vdots \\ V_{a,M}(t) \\ y_1^3(t) \\ \vdots \\ y_M^3(t) \end{bmatrix} \tag{3.55}$$

$$\begin{aligned} \frac{d}{dt}\mathbf{x_{sys}}(t) &= \mathbf{A_{sys}}\mathbf{x_{sys}}(t) + \mathbf{B_{sys}}\mathbf{u_{sys}}(t) \\ &= \mathbf{A_{sys}}\mathbf{x_{sys}} + \mathbf{B_{sys,F_E}}F_E(t) + \mathbf{B_{sys,V_a}}\mathbf{V_a}(t) + \mathbf{B_{sys,nl}}\mathbf{u_{nl}}(t) \end{aligned} \tag{3.56}$$

$$
\frac{d}{dt}\begin{bmatrix} \xi(t) \\ \dot{\xi}(t) \\ y_1(t) \\ \dot{y}_1(t) \\ \vdots \\ y_M(t) \\ \dot{y}_M(t) \\ \mathbf{x_R(t)} \end{bmatrix} =
$$

$$
\begin{bmatrix}
0 & 1 & 0 & 0 & \dots & 0 & 0 & \mathbf{0} \\
\frac{-C_{11}}{M+A_\infty} & 0 & \frac{k_{1,1}}{M+A_\infty} & \frac{b_1}{M+A_\infty} & \dots & \frac{k_{1,M}}{M+A_\infty} & \frac{b_M}{M+A_\infty} & \frac{-\mathbf{C_R}}{M+A_\infty} \\
0 & 0 & 0 & 1 & \dots & 0 & 0 & \mathbf{0} \\
\frac{C_{11}}{M+A_\infty} & 0 & \frac{-k_{1,1}}{M+A_\infty} - \frac{k_{1,1}}{m_1} & \frac{-b_1}{M+A_\infty} - \frac{b_1}{m_1} & \dots & \frac{-k_{1,M}}{M+A_\infty} & \frac{-b_M}{M+A_\infty} & \frac{\mathbf{C_R}}{M+A_\infty} \\
\vdots & \vdots & \vdots & \vdots & \vdots & \vdots & \vdots & \vdots \\
0 & 0 & 0 & 0 & \dots & 0 & 1 & \mathbf{0} \\
\frac{C_{11}}{M+A_\infty} & 0 & \frac{-k_{1,1}}{M+A_\infty} & \frac{-b_1}{M+A_\infty} & \dots & \frac{-k_{1,M}}{M+A_\infty} - \frac{k_{1,M}}{m_M} & \frac{-b_M}{M+A_\infty} - \frac{b_M}{m_M} & \frac{\mathbf{C_R}}{M+A_\infty} \\
\mathbf{0} & \mathbf{B_R} & \mathbf{0} & \mathbf{0} & \dots & \mathbf{0} & \mathbf{0} & \mathbf{A_R}
\end{bmatrix}
\begin{bmatrix} \xi(t) \\ \dot{\xi}(t) \\ y_1(t) \\ \dot{y}_1(t) \\ \vdots \\ y_M(t) \\ \dot{y}_M(t) \\ \mathbf{x_R(t)} \end{bmatrix} +
$$

$$
\begin{bmatrix} 0 \\ \frac{1}{M+A_\infty} \\ 0 \\ \vdots \\ \frac{-1}{M+A_\infty} \\ 0 \\ \frac{-1}{M+A_\infty} \\ \mathbf{0} \end{bmatrix} F_E(t) +
\begin{bmatrix}
0 & \mathbf{0} & 0 \\
\frac{-k_{va,1}}{M+A_\infty} & \dots & \frac{-k_{va,M}}{M+A_\infty} \\
0 & \mathbf{0} & 0 \\
\frac{-k_{va,1}}{M+A_\infty} - \frac{k_{va,1}}{m_1} & \mathbf{0} & 0 \\
\vdots & \ddots & \vdots \\
0 & \mathbf{0} & 0 \\
0 & \mathbf{0} & \frac{-k_{va,M}}{M+A_\infty} - \frac{k_{va,M}}{m_M} \\
\mathbf{0} & \mathbf{0} & \mathbf{0}
\end{bmatrix}
\begin{bmatrix} V_{a,1}(t) \\ \vdots \\ V_{a,M}(t) \end{bmatrix} +
$$

$$
\begin{bmatrix}
0 & \mathbf{0} & 0 \\
\frac{-k_{3,1}}{M+A_\infty} & \dots & \frac{-k_{3,M}}{M+A_\infty} \\
0 & \mathbf{0} & 0 \\
\frac{-k_{3,1}}{M+A_\infty} - \frac{k_{3,1}}{m_1} & \mathbf{0} & 0 \\
\vdots & \ddots & \vdots \\
0 & \mathbf{0} & 0 \\
0 & \mathbf{0} & \frac{-k_{3,M}}{M+A_\infty} - \frac{k_{3,M}}{m_M} \\
\mathbf{0} & \mathbf{0} & \mathbf{0}
\end{bmatrix}
\begin{bmatrix} y_1^3(t) \\ \vdots \\ y_M^3(t) \end{bmatrix} \tag{3.57}
$$

3.6.4 Time-Domain Simulations

One of the uses of state-space modeling is for doing time-domain simulations. The continuous time state-space model of the system can then easily be converted to a discrete time model using standard libraries after specifying some sample rate. Now we will be operating in the sample domain rather than the time domain. The discrete time difference formula given by equation 3.46 uses the states and inputs of the current step n to calculate the next step at $n+1$. Thus simulating the system is relatively simple and can be used to compare the performance of different WEC designs, parameters and control laws.

Chapter 4

Implementation Results

The WEC was designed and simulated in order to understand its performance. Simulations were done on 3 different WECs, a linear WEC, passive non-linear WEC, and non-linear WEC with controls. The following sections will go over the creation of the wave spectrum, and the details and results of each simulation.

4.1 Spectrum

The spectrum that the WEC is simulated in is a Bretschneider Spectrum with significant height of 3.3 m and modal frequency of 0.8 Rad/s. The spectrum was sampled and random phases were used to simulate a wave amplitude signal.

4.2 TLP and Oscillators

All simulated WEC configurations share the same TLP design, same number of oscillators, and the same oscillator mass. The TLP was first chosen to have a cylindrical shape. The submerged portion of the structure under calm water has a diameter of 12 m and a draft of 8 m . This geometry was used as the input to WAMIT and the resulting frequency domain added mass, damping, and excitation plots for motion in surge are shown in figure 4-1. The mass of the TLP was chosen to be is 140,000 kg. Total of 5 oscillators, each having a mass of 8.496 kg were simulated.

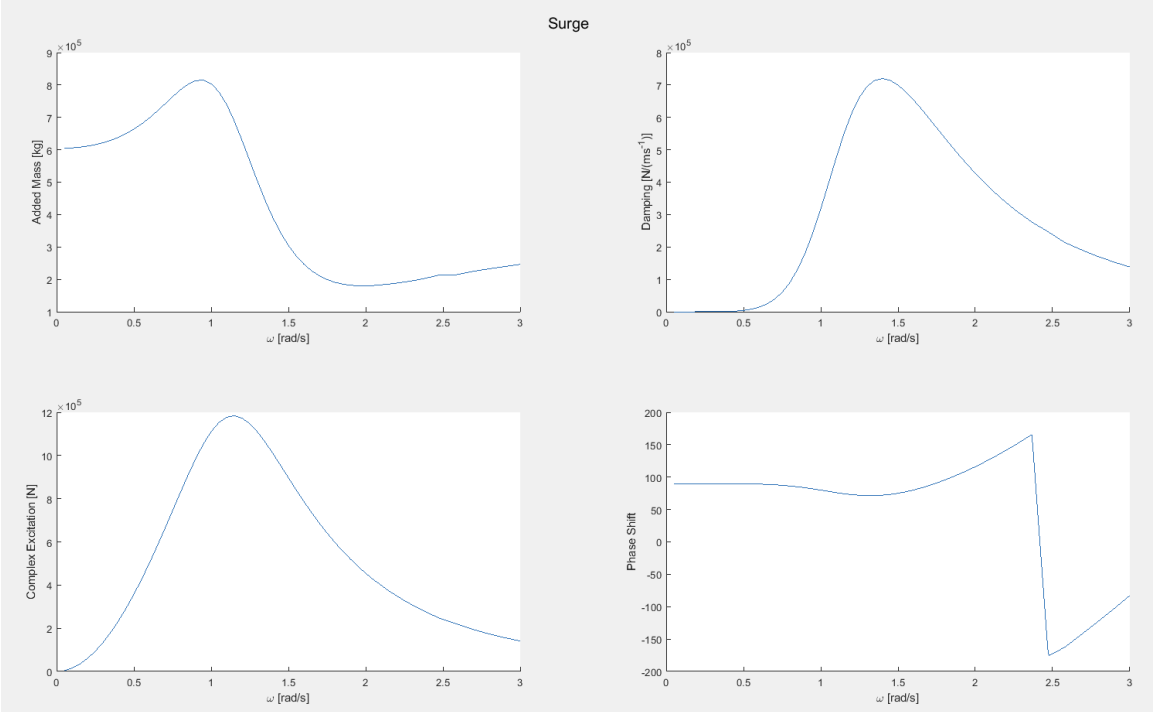

Figure 4-1: Output of WAMIT for a diameter of 12 meters and draft of 8 meters cylindrical buoy in Surge.

4.3 Electromagnetic PTO

All the WEC configurations share the same coil design and PTO, meaning that the coupling coefficient and the coil resistance is the same. However, different configurations might have different values for R_a and R_l.

4.3.1 Resistances

The electromagnetic PTO was designed so that the coils are wrapped around the length of the container. The length of the container with coils wrapped around it is 0.2545 m, which is approximately equal to the length of the levitating stack magnet. The height of coil cross sectional area is equal to 0.0258 m. The coil type was chosen to be AWG 16. Based on the coil cross section dimensions (l_{loop} and h_{loop}) we can calculate the number of loops. The number of loops along the length of the container is $C_{loop} = 197$. The number of layers of loops is $R_{loop} = 22$. Total number loops is $N_{loop} = 4334$. Using the total length of the coil and the resistance characteristics of

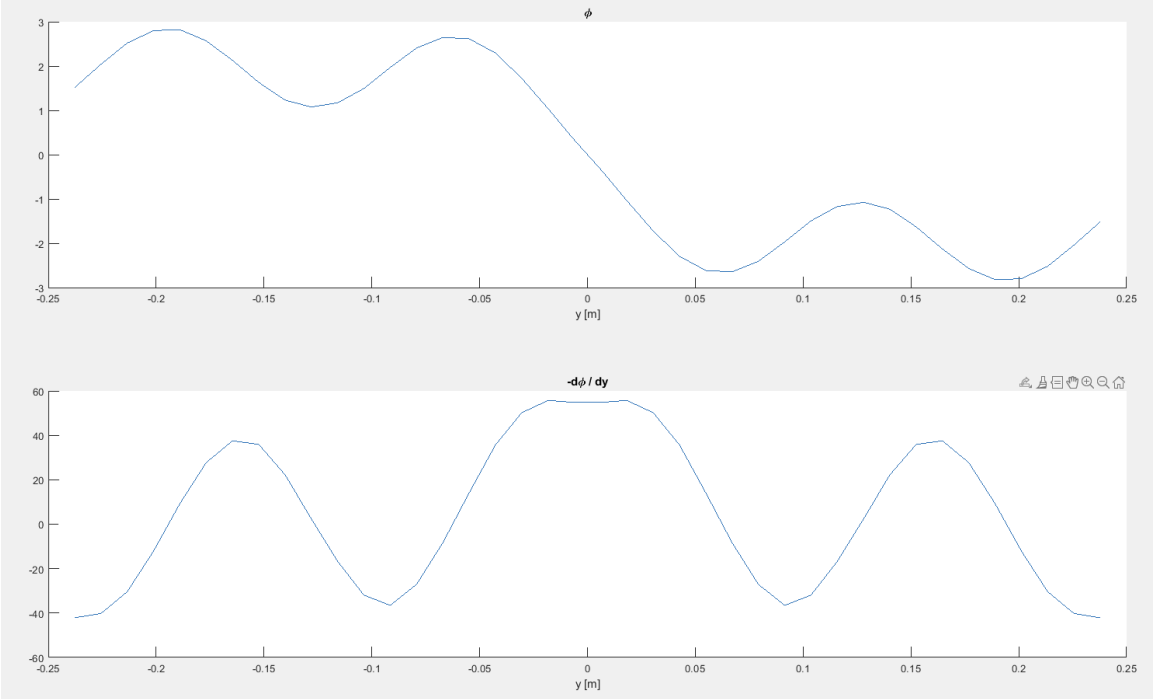

Figure 4-2: The flux linkage ϕ_{mag} (top) and negative derivative of the flux linkage $d\phi/dx$ (bottoms) as a function of the relative displacement of the levitating stack magnet. The coupling coefficient γ_{mag} is the negative derivative of the flux linkage.

the coil type, the total coil resistance was found to be 18.4644 Ω.

4.3.2 Magnetics

The levitating magnet stack was chosen to have four N52 type neodymium magnets, with adjacent magnets facing opposite directions in order to have opposite polarity. Each magnet has a radius of 0.0381 m and length of 0.0381 m. The magnets are kept apart with iron spacers of the same radius and a length of 0.03 m . Considering the densities and geometries of the materials, the total mass of the levitating stack adds up to 8.496 kg. The FEMM software was used to calculate the flux linkage at different points and also the derivative of the flux linkage as shown in figure 4-2. The coupling coefficient can be approximated to be a constant value of $-d\phi/dy(y = 0)$. A slightly lower approximation for the coupling coefficient of 30 was used. The reason why we make this approximation is to make the analysis easier and because the majority of the energy production occurs when the levitating stack is moving across the $y = 0$

position as it moves from one end of the container to the other.

4.4 Linear System

For a linear system, an oscillator can only harvest energy at a narrow bandwidth, thus to capture energy over the entire spectrum, we can place the natural frequencies of each oscillator even across the bandwidth of the spectrum. The frequencies were chosen to be 0.70, 0.9, 1.1, 1.2, and 1.5 Rad/s. The total damping and TLP restoring coefficient was chosen using optimization methods to maximize power while at the same time satisfying some constraints as shown in equation 4.1. The variance constraint from equation 4.1 is set so that the proof mass hitting the edge of the container (represented by $y > y_{max}$) occurs very infrequently. The y_{max} position is at least two standard deviations away. The total damping found is the sum of the electric and mechanical damping. For mechanical damping, friction losses due to viscous damping was considered, but coulomb damping was assumed to be negligible and thus ignored. The mechanical damping was set to 1 $\frac{N\ s}{m}$. Based on this value, the mechanical damping ratios are 0.0841, 0.0654, 0.0535, 0.0453, and 0.0392. The electrical damping is set to the total damping minus the mechanical damping. Considering the mechanical viscous damping and the coil resistance, the impedance condition from equation 3.13 was used to find the optimal load resistance which was found to be 881.5356 Ω.

$$\begin{aligned} &\max_{b_{EM},C_{11}} \text{Power} \\ &b_{EM} >= 0 \\ &\text{Var}(y) < \sqrt{\frac{y_{max}}{2}} \end{aligned} \tag{4.1}$$

4.4.1 Frequency-Domain Analysis

The frequency-domain plot of the TLP response or equation 3.20 is shown in row 2 of figure 4-5. The peak of the TLP response is shown to be close to the modal frequency of the sea spectrum. This allows the natural frequency of the TLP to be aligned with

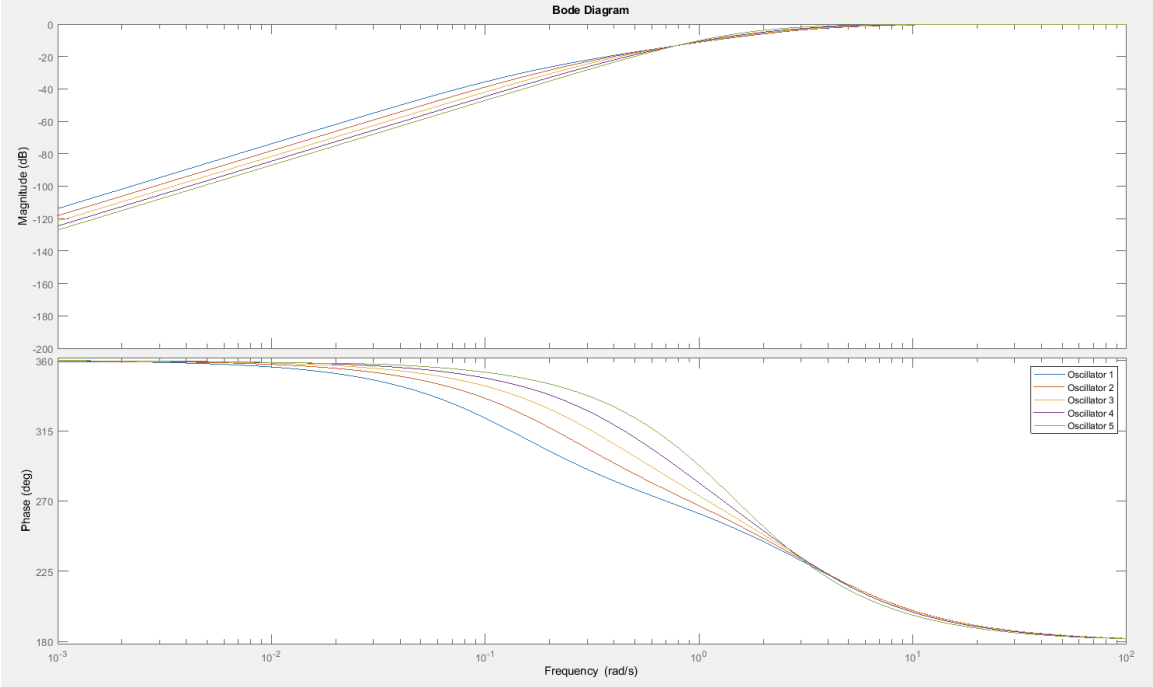

Figure 4-3: The magnitude (top) and phase (bottom) plots of the transfer functions of the linear oscillators with optimal damping under some displacement constraint are shown. Compared with the non-damped system in figure 4-4, the peaks of the response are much smaller in magnitude. The transfer function plotted the one relating $\Xi(\omega)$ to $Y_i(\omega)$ as shown in equation 3.19, where $k_{va} = 0$.

the frequencies in the sea spectrum that contain the most energy. With no damping, the transfer function relating the motion of the TLP to the oscillators is plotted in figure 4-4. This plot corresponds to equation 3.19 but with $\Xi(\omega) = 1$ and $V_a = 0$. Each oscillator is like a narrow bandpass filter and having multiple oscillators at different frequencies can allow us to capture energy over a wider bandwidth. However the undamped system will have very large oscillations and would require a very large space. A damping term was added to constrain the displacements of the oscillators and to harvest power. For a damped system, the resulting frequency domain plots are shown in 4-4. The displacement constraints are now satisfied but at the cost of reducing the power harvested and eliminating the bandpass like behaviour of the oscillators.

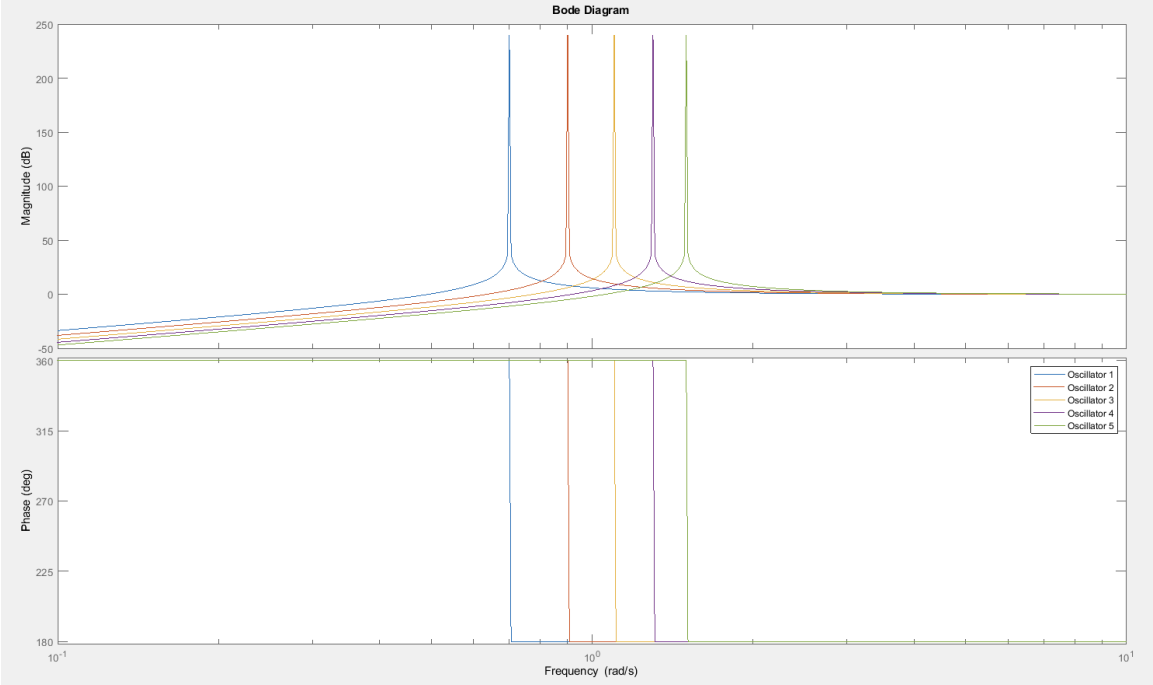

Figure 4-4: The magnitude (top) and phase (bottom) plots of the transfer functions of the linear oscillators with damping set to zero are shown. The transfer function plotted the one relating $\Xi(\omega)$ to $Y_i(\omega)$ as shown in equation 3.19, where $k_{va} = 0$. The natural frequencies of each of the five oscillators are evenly spaced over some frequency range. Each oscillator acts as a narrow bandpass filter that captures energy from different frequencies.

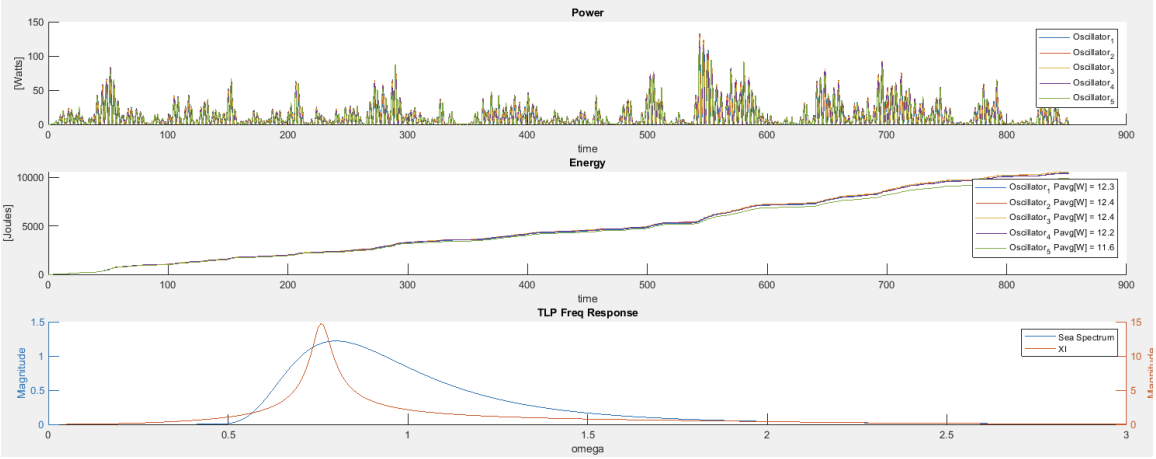

Figure 4-5: A linear WEC with 5 oscillators is simulated in a sea state with a significant height of 3.3 m and modal frequency of 0.8 Rad/s. The power harvested by each oscillator is shown in the top plot. The energy harvested over time by each oscillator is shown in the bottom plot. The magnitude of the frequency response of the TLP and the wave spectrum is shown in the bottom plot. The restoring coefficient of the TLP was optimally chosen, hence the location of the peak of the TLP response coincides with the peak location of the spectrum.

. Details of the dynamics for this simulation are shown in figure 4-6

4.4.2 Time-Domain Simulation

The linear system was simulated in the time domain and the resulting power harvested was calculated to be 62.9976 W, which agrees with the statistical calculation of power using equation 3.35, although this doesn't consider the effects of the oscillator hitting the ends of the container and coming to a stop. The simulated power harvested with these stop constraints is 62.3402 W. The results of that simulation are shown in figures 4-5 and 4-6.

4.4.3 Simulation with Stricter Displacement Constraints

The linear system was simulated again with stricter displacement constraints in order to make a better comparison with the non-linear simulations. The simulated system had a root mean square (RMS) value of 0.37833 m for the position and 0.33474 m/s for the velocity. The resulting average power harvested is 32.5293 W.

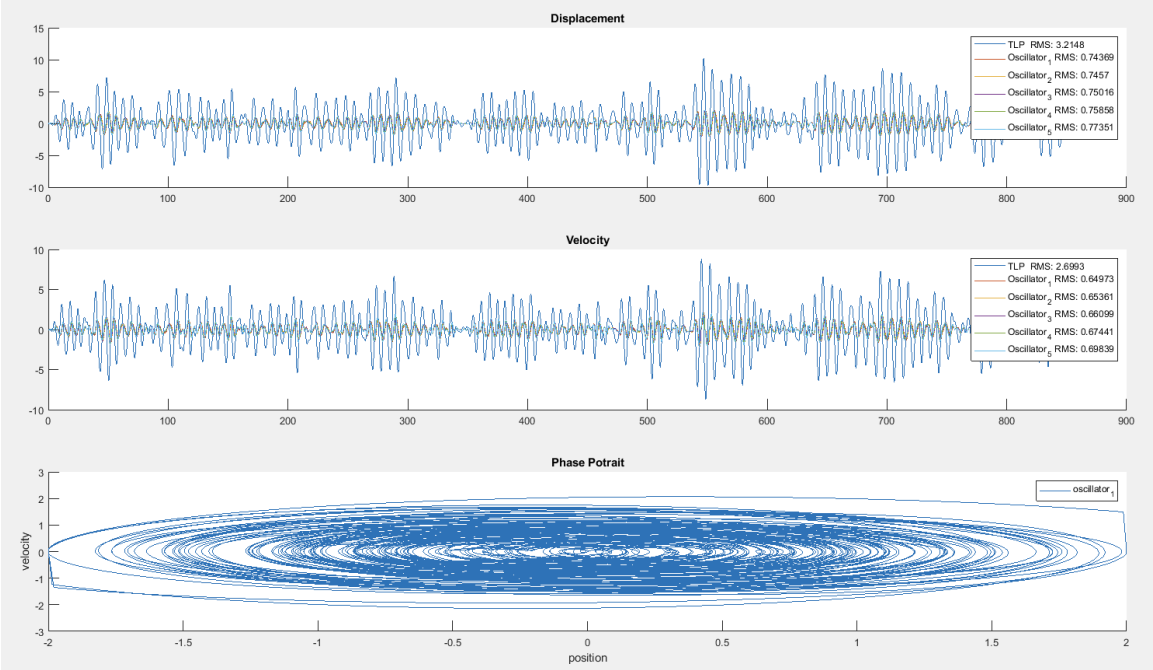

Figure 4-6: A linear WEC with 5 proof masses is simulated in a sea state with a significant height of 3.3 m and modal frequency of 0.8 Rad/s. The displacement (top plot) and velocities (middle plot) of the TLP (blue) and the proof masses (other colors) are shown. The bottom plot shows the phase portrait of the first proof mass oscillator. The phase portrait is an ellipse, with one stable point at velocity and position both equal to 0.

4.5 Passive Non-Linear System

The passive non-linear system was designed and simulated for comparison against the linear system. First the simulation was done with no controls. For the parameters, the mass, coupling coefficient, and coil resistance were the same as the linear case, but the damping is different. Since the optimal damping was chosen in the linear case using linear theory, for the nonlinear case linear theory would not hold any more. The damping was experimentally chosen to optimize the power. The electrical damping was set to 11.3997 $\frac{N\ s}{m}$. From equation 3.3 we can back solve for the required load resistance R_l. The restoring force is now a non-linear, third order polynomial. Using equation 3.42, 3.44, and 3.43, k_1 and k_3 values were obtained after choosing a desired barrier height and stable point. The values chosen for k_1 and k_3 are -91.7568 and 825.8112 respectively. The resulting average power harvested is 13.0633 W. The results of one of the oscillators is shown in figure 4-7 and 4-8. Note that the restoring force is a theoretical restoring force. In order to realize this restoring force, there must be a careful selection of the permanent side magnets and possibly additional springs. Implementing a way to back solve for the side magnet configuration and additional springs is an important future step.

4.6 Non-Linear System with Controls

Now a control circuit is added to the system. The resistance of the additional control branch is R_a = 1500 Ohms. From equation 3.2, the voltage applied is related to the control force generated by a factor k_{va}, which is equal to -0.0157 N/V. The control law follows the one described in section 3.5.2 and the voltage applied was 20 V. The average power generated was 81.3759 W. The simulation results are shown in figure 4-10 and 4-9. If you compare RMS value of the velocity of the oscillator in the non-linear case with controls which is 1.4395 m/s and without controls which is 0.56505 m/s, you can notice that that with the controls the RMS value is much higher. This makes sense because when the control force is turned on, the barrier height is lowered

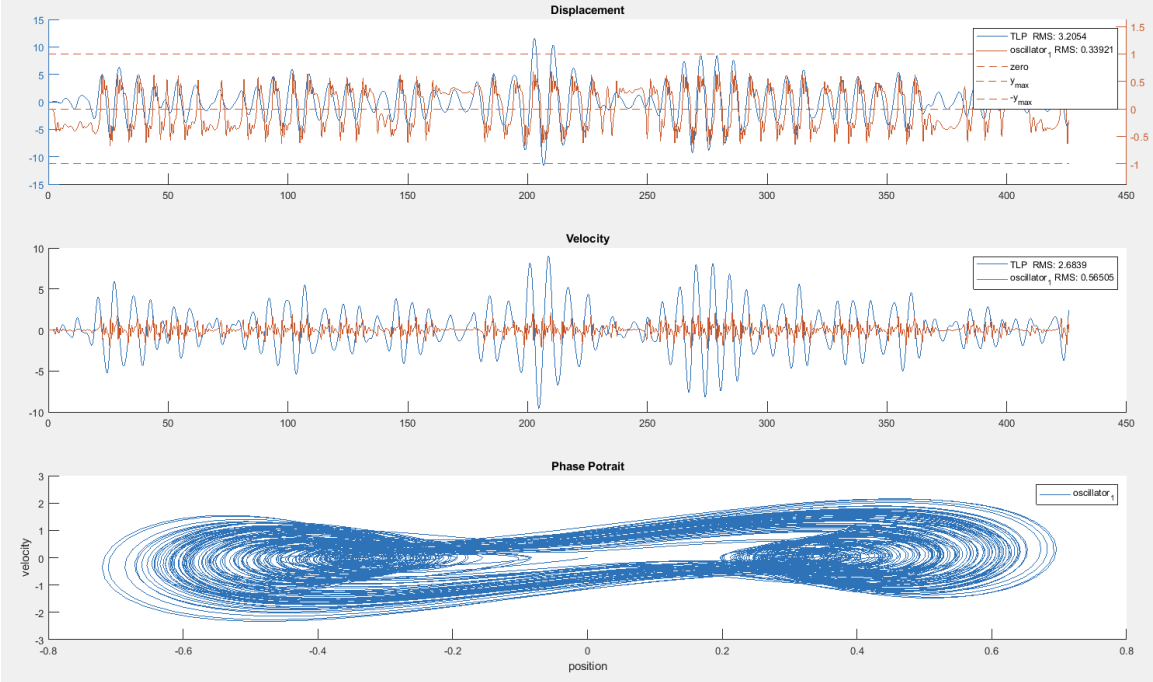

Figure 4-7: A passive non-linear WEC is simulated in a sea state with a significant height of 3.3 m and modal frequency of 0.8 Rad/s. The displacement of one proof mass (red) and the TLP (blue) are shown in the top plot. The dotted lines indicate the $y = 0$ and $\pm y_{max}$ positions to help visualize the position of the proof mass relative to the container. The velocity of the proof mass and TLP are shown in the middle plot. The bottom plot shows the phase portrait of the system. There are two stable points shown as the two circles on the left and right side. The lines connecting the two circles are the states where the proof mass is transitioning between the two stable points. The RMS values of the velocities and positions are shown in the legend of the plots. Figure 4-8 gives more details of the power harvested by this oscillator.

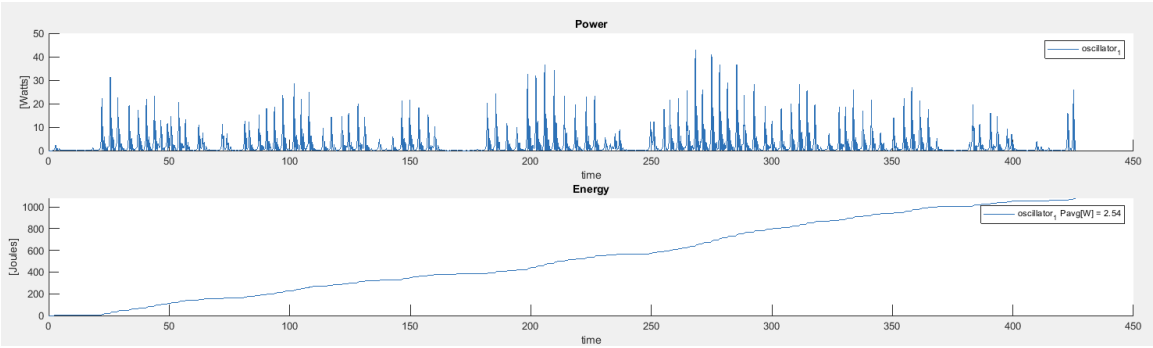

Figure 4-8: The plots of the power harvested (top) and total energy harvested (bottom) by one of the oscillators in the non-linear WEC are shown. The power harvested by all five oscillators is 13.0633 W. Figure 4-7 gives more details on the dynamics of the system.

	RMS Vel	RMS Pos	P_{avg}	Energy Density
Linear	0.69839 m/s	0.77351 m	62.3402 W	5.283 kWh/kg
Linear (Strict Displacement)	0.33474 m/s	0.37833 m	32.5293 W	2.757 kWh/kg
Non-Linear	0.56505 m/s	0.33921 m	13.0633 W	1.107 kWh/kg
Non-Linear with Controls	1.4395 m/s	0.40399 m	81.3759 W	6.896 kWh/kg

Table 4.1: Mass of Buoy is 140,000 kg, Mass of Each Oscillator is 8.496 kg, Number of Oscillators is 5 . The average power is calculated as an average of the power harvested by all the proof masses. The energy density is calculated using the mass of the levitating stack of all of the harvesters and the total energy produced by all the harvesters.

so it is much easier for the proof mass to accelerate to higher speeds as it moves across the container. Since power harvested is correlated with the velocity of the proof mass, controls can be used to increase the velocity by much more.

4.7 Summary of Results

Simulations of the WEC show that for the linear case the power harvested is sensitive to the size of the container. When the system in constrained to a much smaller container, the power harvested is much less. Compared to the linear case, the power harvested for a non-linear WEC without controls is slightly less. Although further optimization for the non-linear WEC can be done to improve its performance. Choosing the restoring force parameters was done using a guess and check method and having a more optimal way to choose those values can improve the performance. Adding controls significantly increases the power harvested by the non-linear system because it can increase the overall RMS value of the velocity without increasing the RMS value of the position by too much. The non-linear WEC with controls is able to generate more power than a linear WEC while having a RMS position value of almost half! This means that the non-linear WEC with controls can be compact while producing just as much power. A summary table of the results are shown in table 4.1. The energy density for the simulated systems are comparable to other wave energy converters in a review of WECs done by Aderinto [1].

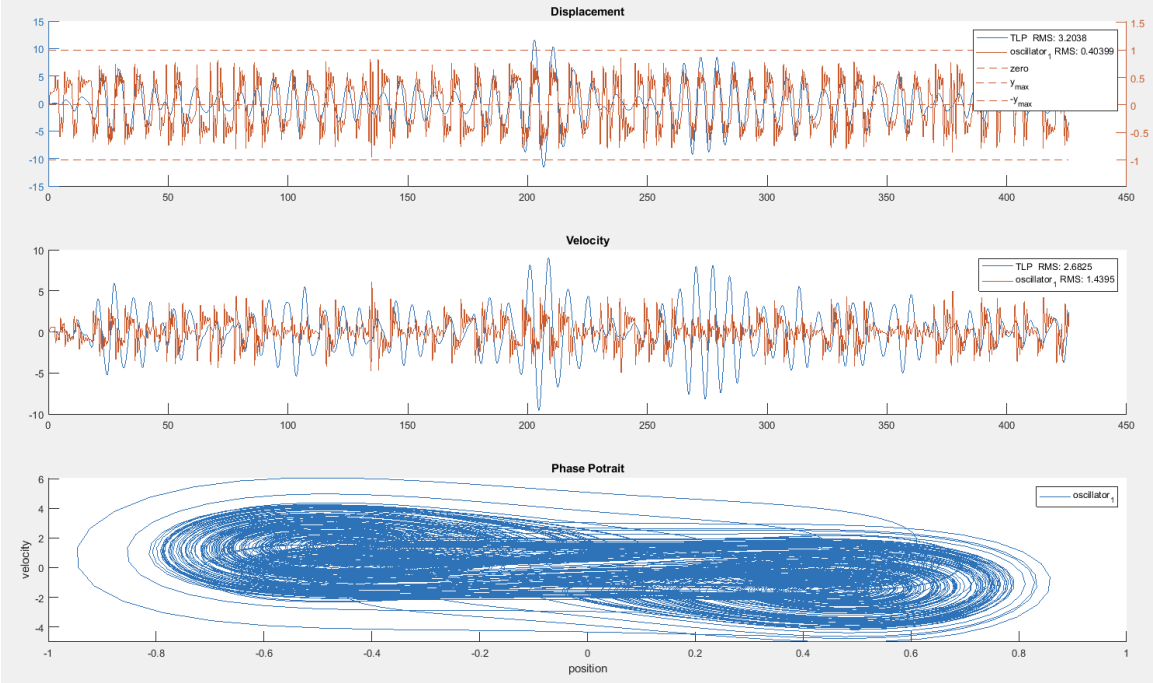

Figure 4-9: A non-linear WEC with controls is simulated in a sea state with a significant height of 3.3 m and modal frequency of 0.8 Rad/s. The displacement of one proof mass (red) and the TLP (blue) are shown in the top plot. The dotted lines indicate the $y = 0$ and $\pm y_{max}$ positions to help visualize the position of the proof mass relative to the container. The velocity of the proof mass and TLP are shown in the middle plot. The bottom plot shows the phase portrait of the system. Two stable points shown as the two circles on the left and right side. The lines connecting the two circles are the states where the proof mass is transitioning between the two stable points. These results can be compared with the results of the non-linear WEC with no controls in figure 4-7. The states where the oscillator is transitioning between the two stable points occur at higher velocities. It also seems as if the stable points have shifted and are not located were the velocity is equal to zero. The RMS values of the velocities and positions are shown in the legend of the plots. Figure 4-10 gives more details of the power harvested by this oscillator

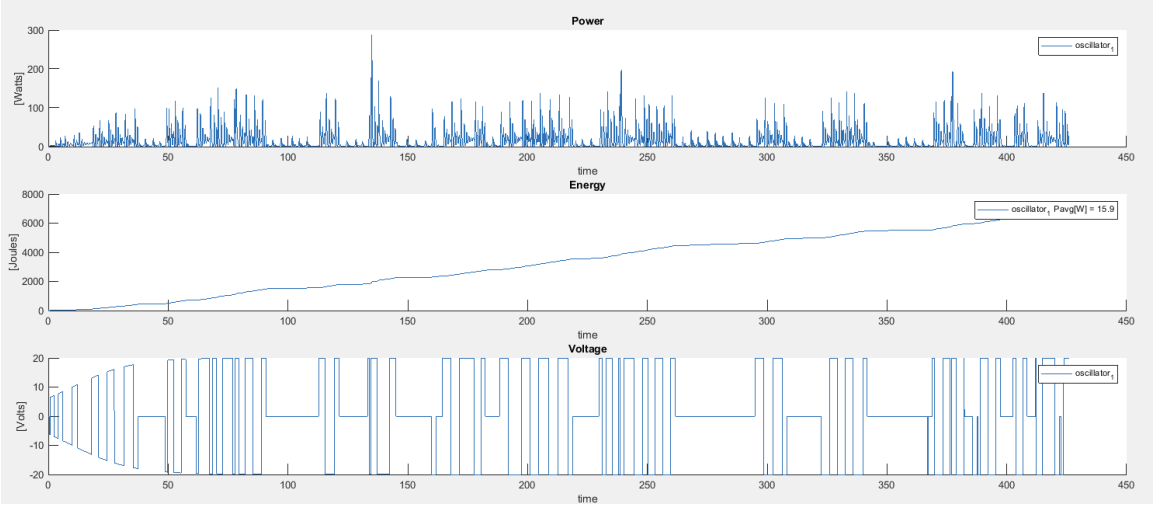

Figure 4-10: The plots of the power harvested (top), total energy harvested (middle) and control voltage (bottom) by one of the oscillators in the non-linear WEC with controls are shown. The power harvested by all five oscillators is 81.3759 W. Figure 4-9 gives more details on the dynamics of the system.

Chapter 5

Future Work

5.1 Permanent Magnet Restoring Force

To further increase the power harvested, the choice of certain parameters should be optimized. The choice of the parameters of the restoring force caused by the permanent magnets is one of those parameters. Improvement on the guess and check method can greatly improve performance. In addition to a better optimization method for the selection of parameters, a method to back solve for the restoring force mechanism given these parameters is required. These results for the non-linear WEC were created using a theoretical restoring force, these restoring forces must be realizable with a certain restoring force mechanism. The restoring force mechanism can contain the permanent side magnets, additional mechanical springs (both linear or non-linear), and other mechanisms. The restoring force can then be shaped by changing the geometries and configurations of those parameters. For example, the type and size of the permanent side magnets can be changed to change the restoring force. Currently there exists a method for extracting the k_1 and k_3 values given the type and size of the side magnets, but there isn't a good way to go in the other direction.

5.2 Forecasting

Forecasting the wave amplitude signal is important because we need it to accurately understand the wave body interaction problem. For example, knowing the excitation force acting on the WEC requires knowing the future wave amplitude signal. Thus a forecasting algorithm is required. Having a forecasting algorithm can help improve the controls of the WEC. Other control laws that can potentially produce more power such as Model Predictive Control requires estimating the future states of the WEC. Methods for forecasting waves for WECs exists, including using support vector machines [8].

5.3 Other Applications

In this thesis we discuss wave energy conversion for the main purposes of electricity production, potentially for supplying energy to the grid. However other interesting applications for WECs with a oscillating proof masses exist. For example, a smaller WEC can be used on board an Autonomous Underwater Vehicle (AUV) to allow it to recharge on site and without re-surfacing.

5.4 Improvements on the Power Take-off Mechanism

The PTO can be optimized to further improve the power harvesting capability. A review of electromagnetic levitating harvested by Carneiro shows that some architectures contain separate windings of coils that are spaced apart from each other rather than one large coil winding [2]. This configuration may have some advantages that can improve the performance of the WEC.

5.4.1 Duffing Oscillator Analysis

The non-linear WEC is a Duffing oscillator and so the frequency domain velocity response can be analyzed [7]. Peak bending of the velocity response occurs when

converting a linear oscillator to a Duffing oscillator. For the certain excitation frequencies, the duffing oscillator can exist in two possible states. Understanding the velocity response of the oscillator can help give us insight to keep the oscillator in the higher energy states more often.

Chapter 6

Conclusion

This thesis has introduced a novel design of a wave energy converter that includes a tension leg platform that contains within it, multiple proof mass oscillators. This wave energy converter uses an electromagnetic power take-off mechanism to convert the motions of the oscillators into electricity. A linear oscillator and a Duffing oscillator with and without a control law were considered. Contributions were made towards understanding the power harvesting capability of this type of wave energy converter. Additionally we have shown that there are advantages to introducing controls to a non-linear WEC that has a bi-stable potential. This wave energy converter is a promising technology but more work needs to be done in order to bring this idea into reality.

Appendix A

Variable Names

$F_R(t)$ Radiation Force

$F_R(\omega)$ Fourier Transform of the Radiation Force

$Z_R(\omega)$ Radiation Impedance

$Z_E(\omega)$ Excitation Force Transfer Function

$f_E(t)$ Excitation Force Kernel

$F_E(t)$ Excitation Force

$Z_I(\omega)$ The Intrinsic Mechanical Impedance

$Xi(\omega)$ Fourier Transform of TLP Displacement

$R_R(\omega)$ Radiation Resistance

$A(\omega)$ Added Mass Function

$h_R(t)$ Radiation Kernel (acceleration)

$k_R(t)$ Radiation Kernel (velocity)

$H_R(\omega)$ Fourier Transform of Radiation Kernel (acceleration)

$K_R(\omega)$ Fourier Transform of Radiation Kernel (velocity)

B_{mag} Magnetic Flux

ϵ_{mag} Electromotive Force

γ_{mag} Magnetic Coupling Coefficient or also known as the Transduction Factor

b_m Mechanical Damping

F_i Force Induced via Lenz's Law

R_c, R_l, R_a Coil Resistance, Load Resistance and Control Resistance

$F_L(\omega)$ Fourier Transform of the Load Force

I_c, I_l, and I_a Current Through the Coils, Load and Control Branch

$S(\omega)$ Ocean Spectrum

ω_m Modal Frequency

$s(t)$ Wave Amplitude Signal

$H_{1/3}$ Significant Wave Height

$\mathcal{A}_{\mathbf{sys}}, \mathcal{B}_{\mathbf{sys}}, \mathcal{C}_{\mathbf{sys}}, \mathcal{D}_{\mathbf{sys}}$ Discrete Time State Space Matrices for WEC System

$\mathbf{A}_{\mathbf{sys}}, \mathbf{B}_{\mathbf{sys}}, \mathbf{C}_{\mathbf{sys}}, \mathbf{D}_{\mathbf{sys}}$ Continuous Time State Space Matrices for WEC System

M Number of Oscillators

O Order of the Radiation Approximation

N_{mag} Number of Magnets in Each Levitating Magnet Stack

b_M Mechanical Damping

b_E Electromagnetic Damping

k_{va} Control Coefficient

k_1 and k_3 Oscillator Restoring Force Coefficients

C_{11} TLP Restoring Coefficient

r_{wire} Radius of the Wire

Ω_{wire} Resistance Per Meter of Wire

$J(t)$ Current Density

l_{wire} Total Wire Length of the Coils

r_{box} The Radius of the Container/ Box Containing the Proof Mass

l_{loop} the Length of the Cross Sectional Area of the Coils

h_{loop} the Height of the Cross Sectional Area of the Coils

b_M Mechanical Damping of Oscillator

b_E Electrical Damping of Oscillator

b_{EM} Total Damping of Oscillator

$Y(\omega)$ Frequency Response of Oscillator.

k_{tether} Spring Constant of Tethers

θ_{tether} The Angle of the Tethers to the Ocean Floor

$y, \dot{y}$ Relative Position and Velocity of Proof Mass

$\xi, \dot{\xi}$ Relative Position and Velocity of TLP

Φ Power Spectral Density or Power Spectral Density

ϕ_{mag} Induced Flux via Electromagnetic Induction

ϵ_{mag} Electromotive Force

d_{sep} Seperation Distance of Levitating Stack Magnets

$A(\infty)$ or A_∞ Infinite Added Mass

$V_a(t)$ and $V_a(\omega)$ The Applied Voltage and its Fourier Transform

Bibliography

[1] Tunde Aderinto and Hua Li. Ocean wave energy converters: Status and challenges. *Energies*, 11(5), 2018.

[2] Pedro Carneiro, Marco P Soares dos Santos, André Rodrigues, Jorge AF Ferreira, José AO Simões, A Torres Marques, and Andrei L Kholkin. Electromagnetic energy harvesting using magnetic levitation architectures: A review. *Applied Energy*, 260:114191, 2020.

[3] Carlos (Casanovas Bermejo) Casanovas. Advanced controls for floating wind turbines, 2014.

[4] Johannes Falnes. *Ocean Waves and Oscillating Systems*. Cambridge University Press, 2002.

[5] Einar Halvorsen, Cuong Phu Le, PD Mitcheson, and Eric M Yeatman. Architecture-independent power bound for vibration energy harvesters. In *Journal of Physics: Conference Series*, volume 476, page 012026. IOP Publishing, 2013.

[6] Ashkan Haji Hosseinloo and Konstantin Turitsyn. Non-resonant energy harvesting via an adaptive bistable potential. *Smart Materials and Structures*, 25(1):015010, 2015.

[7] Yu Jia. Review of nonlinear vibration energy harvesting: Duffing, bistability, parametric, stochastic and others. *Journal of Intelligent Material Systems and Structures*, 31(7):921–944, 2020.

[8] Yu Ma et al. *Machine learning in ocean applications: wave prediction for advanced controls of renewable energy and modeling nonlinear viscous hydrodynamics*. PhD thesis, Massachusetts Institute of Technology, 2020.

[9] Christine Miller. A brief history of wave and tidal energy experiments in san francisco and santa cruz. *Western Neighborhoods Projects. Western Neighborhoods Project*, 3, 2004.

[10] Alan V Oppenheim and George C Verghese. *Signals, Systems and Inference: Class Notes for 6.011, Introduction to Communication, Control and Signal Processing*. 2010.

[11] James Prendergast, Mingfang Li, and Wanan Sheng. A study on the effects of wave spectra on wave energy conversions. *IEEE Journal of Oceanic Engineering*, 45(1):271–283, 2018.

[12] Dirk Spreemann and Yiannos Manoli. *Electromagnetic vibration energy harvesting devices: Architectures, design, modeling and optimization*, volume 35. Springer Science & Business Media, 2012.

[13] Siyuan Zhan and Guang Li. Linear optimal noncausal control of wave energy converters. *IEEE Transactions on Control Systems Technology*, 27(4):1526–1536, 2018.